Quantification of evaporative loss of volatile metals from planetary cores and metal-rich planetesimals

Steenstra, E.S.; Renggli, C.J. ; Berndt, J.; Klemme, S.

Important note
To cite this publication, please use the final published version (if applicable).
Please check the document version above.

Quantification of evaporative loss of volatile metals from planetary cores and metal-rich planetesimals

E.S. Steenstra [a,b,*], C.J. Renggli [b,c], J. Berndt [b], S. Klemme [b]

[a] Faculty of Aerospace Engineering, Technische Universiteit Delft, the Netherlands
[b] Institute of Mineralogy, University of Münster, Germany
[c] Max Planck Institute for Solar System Research, Göttingen, Germany

ARTICLE INFO

ABSTRACT

The processes responsible for the isotopic compositions and abundances of volatile elements in the early solar system remain highly debated. Orders of magnitude variation of (highly) volatile elements exist between different magmatic iron meteorite groups, but it is unclear to what extent their depletions can be explained by evaporation from metal melts during parent body accretion and/or subsequent break up. To this end, we present 86 new evaporation experiments with the aim of constraining the volatility of most volatile metals from metallic melts. The results confirm the previously proposed important effects of S in metal melt on the volatility of the elements of interest governed by their S-loving or S-phobic behavior. Nominally S-loving elements In, Sn, Te, Pb and Bi are significantly more volatile in Fe melt relative to FeS liquid, whereas nominally S-avoiding elements Ga and Sb are more volatile in FeS liquid relative to Fe melt, at a given pressure and temperature. The newly derived volatility sequences for S-free/poor and S-rich metallic melts were also compared with commonly used volatility models based on condensation temperatures. The results indicate significant differences between the latter, including the much more volatile behavior of Te, relative to Se, in both explored bulk compositions, which are traditionally assumed to be equally volatile. The (minimum) degree of volatile element depletion due to evaporation was quantified using the new experimental results and models. A comparison between the volatile element depletions in magmatic iron meteorites and the predicted depletions appropriate for evaporation from Fe melts shows that the latter depletions can be easily reconciled with (an) evaporation event(s). Altogether, the new data and models will provide an important framework when more accurate and precise estimates of magmatic iron meteorite bulk volatile element contents are available.

1. Introduction

The chemical composition of magmatic iron meteorites provides key perspectives into planetary accretion processes, including the architecture of and distribution of material within the early solar system (Rubin, 2018; Grewal et al., 2024), crystallization of planetary cores (Campbell and Humayun, 2005; Chabot and Zhang, 2021) and high-temperature processing of planetary materials (Fehr et al., 2005; Kruijer et al., 2014; Matthes et al., 2018; Gargano and Sharp, 2019; Hirschmann et al., 2021). Magmatic iron meteorites are mainly grouped according to their trace element compositions and could represent the cores of more than 60 planetesimals (Goldstein et al., 2009). The degree of depletion in volatile elements relative to their inferred building blocks increases significantly from type I to IV iron meteorites (Scott and Wasson, 1975).

However, the origin of these variable extents of elemental depletions remains highly debated. The three major hypotheses attribute the volatile loss to inheritance of depletions from incorporation of chondritic precursor materials (i.e., incomplete condensation in the nebula or nebular processing; Sears, 1978; Wai and Wasson, 1979; Scott, 1979; Campbell and Humayun, 2005; Chen et al., 2013), loss during accretion and/or by volatile loss during catastrophic impact disruptions of their parent bodies (e.g., Rasmussen et al., 1984; Campbell and Humayun, 2005; Yang et al., 2008; Horan et al., 2012; Matthes et al., 2018; Jordan et al., 2019). The measured abundance of Cd, a nominally highly volatile element given its very low 50 % condensation temperature ($T_{50\%} =$ ~500 to ~650 K, Lodders, 2003; Wood et al., 2019), may point to decoupling of ''highly'' volatile elements (e.g., Cd, Pb, Bi) and ''moderately'' volatile elements (e.g., Ga, Cu, Ge) in magmatic iron

---

meteorites (Kruijer et al., 2014). This may suggest that the highly volatile elements such as Zn, In, Cd, Pb, Bi may not have accreted initially given their very low $T_{50\%}$ (Chen et al., 2013; Corrigan et al., 2022), whereas moderately volatile elements such as Ga and Ag could have been lost primarily during or following parent body accretion (e.g., Campbell and Humayun, 2005, Horan et al., 2012; Kruijer et al., 2014; Matthes et al., 2018).

Evaporation of volatile elements from a S-poor or S-rich metal melt could have occurred during or following (a) catastrophic impact(s) on the parent body, resulting in melting of the metal core and/or exposing a liquid core to space, as proposed for the IVA and IVB parent bodies, from geochemistry and reconstructed anomalous thermal histories (e.g., Yang et al., 2008, 2010; Matthes et al., 2018; Spitzer et al., 2021). Indeed, several magmatic iron meteorite groups record complex collisional histories, including the IIIAB (Matthes et al., 2020) and IVA (Haack et al., 1996; Rubin et al., 2022) groups, as implied from prominent clusters in cosmic-ray exposure ages (Yang et al., 2008). Given the early and fast cooling of the latter meteorite suites, the insulating mantle was likely removed, exposing the liquid core directly to space (e.g., Matthes et al., 2020).

Evaporative loss would also be consistent with previous models that suggested that the IVB parent body (and likely other magmatic iron meteorite parent bodies) could have experienced internal temperatures exceeding 1760 K (Campbell and Humayun, 2005), which would yield extensive if not complete melting of the core (Chabot and Haack, 2006). Nevertheless, Campbell and Humayun (2005) proposed that the low moderately volatile element contents in group IVB are due to volatility processing in a nebular setting, instead of in the parent body. The slightly heavier average Fe isotopic composition (δ^{57}Fe ~0.13 ‰) of the group IIIAB irons, relative to chondrites, has been interpreted to (partly) reflect evaporation of Fe from a silicate and/or metal melt during or shortly after accretion of their parent bodies (Jordan et al., 2019). However, the δ^{57}Fe values of magmatic iron meteorites could also be solely explained by magmatic differentiation during core crystallization (e.g., Ni et al., 2020). The Zn isotopic composition of several magmatic iron meteorite parent suites may also point to (a) different type(s) of depletion process(es) besides evaporation, such as incomplete condensation (Chen et al., 2013).

Given the enigmatic nature of volatile element depletions in magmatic iron meteorites, experimentally derived evaporation data for other volatile elements applicable to metal melts are clearly required (Chabot and Zhang, 2021; Corrigan et al., 2022; Rubin et al., 2022; Grewal and Asimow, 2023). Although the evaporation behavior of Cu, Ge and Ag and several nominally refractory elements from metal melts was recently constrained (Steenstra et al., 2023), the behavior of other volatile elements remains experimentally unexplored. Evaporative loss of volatiles from metal melts may also be directly applicable to metal-rich asteroids such as 16 Psyche, depending on eruptive style and extent of melting on such parent bodies.

We recently showed that the elemental depletion patterns of Cu, Ge and Ag observed for the IVB magmatic iron meteorites (Campbell and Humayun, 2005) can be easily explained by evaporative loss from a S-free or S-poor Fe-rich melt under vacuum (0.0004) bar for a wider range of evaporation times and temperatures (Steenstra et al., 2023). The experimental data also showed the key role of S on the volatility and evaporation rates of these elements. To quantitatively assess to what extent evaporation of an exposed core could explain the abundance of other volatile elements in magmatic iron meteorites, data on their volatility in metallic systems are clearly required. To this end, we present the first evaporation data for a large suite of volatile metals (Zn, Ga, Se, Cd, In, Sn, Sb, Te, Pb, Bi), as a function of pressure, temperature and composition. The new data, combined with the previous study, will then be used to obtain a volatility sequence that is, for the first time, directly applicable to metal melts. This sequence is subsequently compared with condensation temperature volatility models (Wood et al., 2019) that are commonly used for studying volatile element depletions in magmatic

iron meteorites (e.g., Chabot and Zhang, 2021).

2. Methods

2.1. Experimental

Two types of metallic mixtures, Fe + traces, FeS+traces, were melted in a gas mixing furnace at the Institute of Mineralogy, University of Münster at two pressures (~0.0002 and 1 bar) for 5–120 min at 1573–1773 K (Table 1) (see also Steenstra et al., 2023). Starting materials were obtained by mixing high-purity FeS or Fe powders with ~0.1 mol % of high-purity Ni, Zn, Ga, Se, Cd, In, Sn, Sb, Te, Pb and Bi powders. The starting materials were mixed in an agate mortar under ethanol for at least 30 min to ensure homogeneous starting materials. The trace element-bearing Fe and FeS powders were subsequently pressed as pellets with diameters of 3 mm and loaded in separate, ~2 cm long graphite buckets (~4–5 mm O.D., ~3 mm I.D.) that in turn were placed in a larger single graphite bucket of ~4–5 cm long and 2–3 cm wide. Experiments run at 1 bar were flushed with pure CO and the use of a graphite bucket buffered the experiments at the graphite − CO (GCO) buffer (Steenstra et al., 2023). Temperatures were monitored and controlled using a type B thermocouple and a Eurotherm 3508 (Schneider Electric, Germany) programmable controller. The estimated temperature uncertainties are <5 degrees. Vacuum was attained in the furnace by attaching an Alcatel vacuum pump to the lower end of the vertical furnace tube (alumina) and sealing the gas-input valve at the top of the furnace. The pressure was monitored with an Edwards vacuum gauge. For additional experimental details, the reader is referred to Steenstra et al. (2023). After the experiments the samples were embedded in epoxy resin and polished using various grades of SiC sandpaper and polycrystalline diamond spray. The samples were carbon-coated for imaging and chemical analyses of major elements by electron microprobe, after which they were measured for trace elements by laser ablation inductively coupled plasma mass spectrometry (LA-ICP-MS).

2.2. Analytical

Experimental run products were imaged and analyzed using the JEOL JXA 8530F electron microprobe at the University of Münster using the approach of Steenstra et al. (2023) (Tables S1, S2; Steenstra, 2024). All metal and sulfide phases were analyzed using a defocused beam of 5–20 μm, depending on the available surface area, with beam currents of 15–20 nA and an accelerating voltage of 15 kV. The analysis points were set in lines and/or raster grids and special care was taken to avoid analyses of areas close to the edge of phases and/or surrounding capsule materials. Counting times were 10–30 s on peak and 5–15 s on each background. Analyses for sulfide liquids and silicate melts were calibrated on well-characterized natural and synthetic micro-analytical reference materials. The standards used for metal and sulfide analyses were hypersthene for Si, pyrite for Fe and S, MgO for O and pure metal standards for Ti, Mn, Cr, Ni. Trace elements were subsequently measured using LA-ICP-MS at Münster University. All LA-ICP-MS measurements were performed using a 193 nm ArF excimer laser (Analyte G2, Photon Machines) with a repetition rate of 10 Hz and energy of ~3–4 J/cm^2 throughout the entire session and beam sizes ranging between 25–110 μm, depending on the area available for measurements. The preferred beam size used throughout the study was 110 μm, but in case of S-poor Fe blobs in FeS liquids beam sizes were in some cases reduced to 25 μm. The following masses were monitored: ^{24}Mg, ^{27}Al, ^{29}Si, ^{43}Ca, ^{49}Ti, ^{51}V, ^{53}Cr, ^{55}Mn, ^{56}Fe, ^{59}Co, ^{60}Ni, ^{61}Ni, ^{63}Cu, ^{65}Cu, ^{66}Zn, ^{71}Ga, ^{73}Ge, ^{75}As, ^{77}Se, ^{95}Mo, ^{101}Ru, ^{105}Pd, ^{107}Ag, ^{111}Cd, ^{115}In, ^{118}Sn, ^{121}Sb, ^{125}Te, ^{182}W, ^{185}Re, ^{193}Ir, ^{205}Tl, ^{208}Pb and ^{209}Bi. As discussed in Steenstra et al. (2023), representative reference materials appropriate for Fe and FeS solids containing comparable amounts of C and the elements of interest are not available. Starting materials were therefore

Table 1

Experimental run conditions.

	T (K)	P (bar)	Time (min)	Starting comp [a]	Phases [b]	Comments
ESS-1-135Fe	1623	1	15	Fe A	Fe	Performed together with ESS-1-135 FeS; not fully liquid [c]
ESS-1-135 FeS	1623	1	15	FeS A	FeS	Performed together with ESS-1-135 Fe
ESS-1-135A Fe	1623	1	15	Fe A	Fe	Not fully liquid
ESS-1-135A FeS	1623	1	15	FeS A	FeS	–
ESS-1-1375 Fe	1648	1	15	Fe A	Fe	Performed together with ESS-1-1375 FeS, not fully liquid
ESS-1-1375 FeS	1648	1	15	FeS A	FeS	Performed together with ESS-1-1375 Fe
ESS-1-140A Fe	1673	1	15	Fe A	Fe	Performed together with ESS-1-140A FeS, not fully liquid
ESS-1-140A FeS	1673	1	15	FeS A	FeS	Performed together with ESS-1-140A Fe
ESS-1-140A1 Fe	1673	1	15	Fe A	Fe	Not fully liquid
ESS-1-140A1 FeS	1673	1	15	FeS A	FeS	–
ESS-1-140B Fe	1673	1	30	Fe A	Fe	Performed together with ESS-1-140B FeS, not fully liquid
ESS-1-140B FeS	1673	1	30	FeS A	FeS	Performed together with ESS-1-140B Fe
ESS-1-140B1 Fe	1673	1	30	Fe A	Fe	Not fully liquid
ESS-1-140B1 FeS	1673	1	30	FeS A	FeS	–
ESS-1-140C Fe	1673	1	60	Fe A	Fe	Performed together with ESS-1-140C FeS, not fully liquid
ESS-1-140C FeS	1673	1	60	FeS A	FeS	Performed together with ESS-1-140C Fe
ESS-1-140C1 Fe	1673	1	60	Fe A	Fe	Not fully liquid
ESS-1-140C1 FeS	1673	1	60	FeS A	FeS	–
ESS-1-140D Fe	1673	1	120	Fe A	Fe	–
ESS-1-140D FeS	1673	1	120	FeS A	FeS	–
ESS-1-140E Fe	1673	1	5	Fe A	Fe	Not fully liquid
ESS-1-140E FeS	1673	1	5	FeS A	FeS	–
ESS-1-140F Fe	1673	1	10	Fe A	Fe	Not fully liquid
ESS-1-140F FeS	1673	1	10	FeS A	FeS	–
ESS-1-140G FeS	1673	1	22.5	FeS A	FeS	–
ESS-1-140H FeS	1673	1	45	FeS A	FeS	–
ESS-1-1425 Fe	1698	1	15	Fe A	Fe	–
ESS-1-1425 FeS	1698	1	15	FeS A	FeS	–
ESS-1-145 Fe	1723	1	15	Fe A	Fe	Performed together with ESS-1-145A FeS, not fully liquid
ESS-1-145 FeS	1723	1	15	FeS A	FeS	Performed together with ESS-1-145A Fe
ESS-1-145A Fe	1723	1	15	Fe A	Fe	Not fully liquid
ESS-1-145A FeS	1723	1	15	FeS A	FeS	–
ESS-1-150A Fe	1773	1	15	Fe A	Fe	Performed together with ESS-1-150A FeS
ESS-1-150A FeS	1773	1	15	FeS A	FeS	Performed together with ESS-1-150A Fe
ESS-1-150AA Fe	1773	1	15	Fe A	Fe	–
ESS-1-150A1 Fe	1773	1	15	Fe A	Fe	–
ESS-1-150A1 FeS	1773	1	15	FeS A	FeS	–
ESS-1-150A2 Fe	1773	1	15	Fe A	Fe	–
ESS-1-150B Fe	1773	1	5	Fe A	Fe	Performed together with ESS-1-150B FeS, not fully liquid
ESS-1-150B FeS	1773	1	5	FeS A	FeS	Performed together with ESS-1-150B Fe
ESS-1-150BB Fe	1773	1	5	Fe A	Fe	–
ESS-1-150B2 FeS	1773	1	5	FeS A	FeS	–
ESS-1-150C Fe	1773	1	10	Fe A	Fe	Performed together with ESS-1-150C FeS, not fully liquid
ESS-1-150C FeS	1773	1	10	FeS A	FeS	Performed together with ESS-1-150C Fe
ESS-1-150CC Fe	1773	1	10	Fe A	Fe	–
ESS-1-150C2 FeS	1773	1	10	FeS A	FeS	–
ESS-1-150C1 Fe	1773	1	10	Fe A	Fe	Not fully liquid
ESS-1-150C3 FeS	1773	1	10	FeS A	FeS	–
ESS-1-150D Fe	1773	1	30	Fe A	Fe	Performed together with ESS-1-150D FeS
ESS-1-150D1 FeS	1773	1	30	FeS A	FeS	Performed together with ESS-1-150D Fe
ESS-1-150DD Fe	1773	1	30	Fe A	Fe	–
ESS-1-150D2 FeS	1773	1	30	FeS A	FeS	–
ESS-1-150E Fe	1773	1	60	Fe A	Fe	Performed together with ESS-1-150E FeS
ESS-1-150E FeS	1773	1	60	FeS A	FeS	Performed together with ESS-1-150E Fe
ESS-1-150E1 Fe	1773	1	60	Fe A	Fe	–
ESS-1-150E2 FeS	1773	1	60	FeS A	FeS	–
ESS-1-150G FeS	1773	1	45	FeS A	FeS	–
ESS-1-150H FeS	1773	1	22.5	FeS A	FeS	–
ESS-V-130 Fe	1573	0.0002	15	Fe A	Fe	–
ESS-V-130 FeS	1573	0.0002	15	FeS A	FeS	–
ESS-V-135 Fe	1598	0.0002	15	Fe A	Fe	–
ESS-V-135 FeS	1598	0.0002	15	FeS A	FeS	–
ESS-V-1375 Fe	1623	0.0002	15	Fe A	Fe	–
ESS-V-1375 FeS	1623	0.0002	15	FeS A	FeS, S-poor Fe-rich alloy	–
ESS-V-140A Fe	1673	0.0002	15	Fe A	Fe	–
ESS-V-140A FeS	1673	0.0002	15	FeS A	FeS	–
ESS-V-140B Fe	1673	0.0002	30	Fe A	Fe	–
ESS-V-140B FeS	1673	0.0002	30	FeS A	FeS, S-poor Fe-rich alloy	–
ESS-V-140C Fe	1673	0.0002	60	Fe A	Fe	–
ESS-V-140C FeS	1673	0.0002	60	FeS A	FeS, S-poor Fe-rich alloy	–
ESS-V-1425 Fe	1698	0.0002	15	Fe A	Fe	–
ESS-V-1425 FeS	1698	0.0002	15	FeS A	FeS, S-poor Fe-rich alloy	–
ESS-V-145 Fe	1723	0.0002	15	Fe A	Fe	–
ESS-V-145 FeS	1723	0.0002	15	FeS A	FeS, S-poor Fe-rich alloy	–

Table 1 (*continued*)

	T (K)	P (bar)	Time (min)	Starting comp [a]	Phases [b]	Comments
ESS-V-150A Fe	1773	0.0002	15	Fe A	Fe	–
ESS-V-150B Fe	1773	0.0002	5	Fe A	Fe	–
ESS-V-150B FeS	1773	0.0002	5	FeS A	FeS	–
ESS-V-150C Fe	1773	0.0002	10	Fe A	Fe	–
ESS-V-150D Fe	1773	0.0002	30	Fe A	Fe	–
ESS-V-150E Fe	1773	0.0002	60	Fe A	Fe	–

[a] FeS A=FeS+0.1 mol % of Ni, Zn, Ga, Se, Cd, In, Sn, Sb, Te, Pb, Bi; Fe A=Fe + 0.1 mol % of Ni, Zn, Ga, Se, Cd, In, Sn, Sb, Te, Pb, Bi.

[b] FeS=FeS liquid; Fe = Fe liquid; S-poor Fe-rich alloy = immiscible S-poor Fe liquid.

[c] The estimated C content, derived from consideration of EPMA totals, implies that some of the runs did not experience complete melting.

synthesized at high *P-T* conditions (1.5 GPa and 1873 K) in graphite capsules in an end-loaded piston cylinder apparatus at the University of Münster. At these conditions, no volatility-related loss of the elements of interest is expected. Measurements of the run products confirmed that the Fe liquid synthesized at high *P-T* contained comparable amounts of C relative to most of the evaporated samples, as they are both buffered by the graphite capsule. However, some lower-temperature experiments did not experience complete melting, resulting in overall lower C contents (Table S2). The FeS liquids were found to contain comparable O contents, and the textures of both FeS and Fe liquids of the high *P-T* synthesized samples and evaporated samples were generally similar.

Measurements were conducted using the NIST 610 glass as an
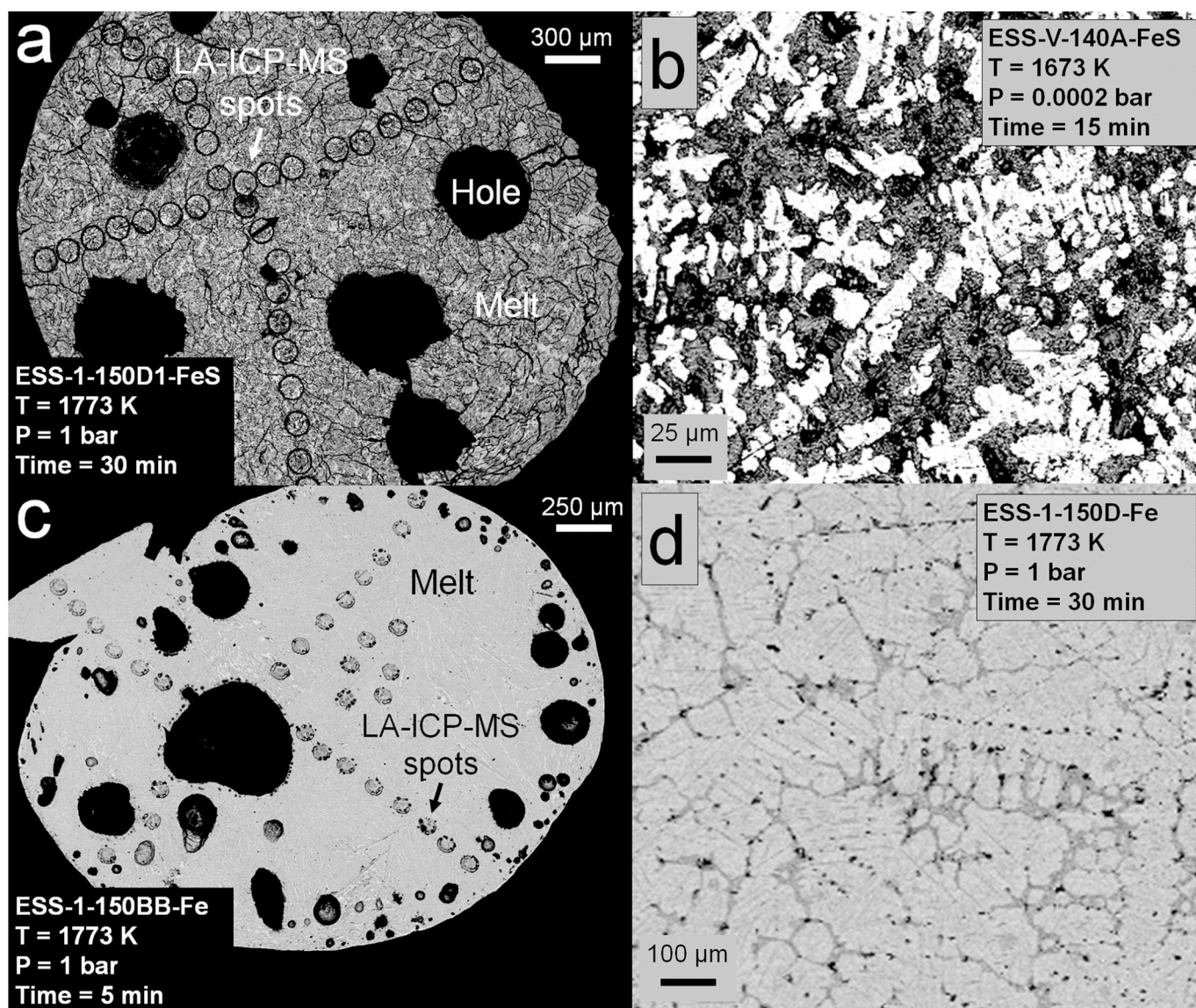
Fig. 1. Backscattered electron images of FeS and Fe samples. Panel **(a)** shows an overview of a typical FeS experimental run product, ESS-1-150D1-FeS, conducted at 1 bar and 1773 K for 30 min. Clearly visible are the LA-ICP-MS spot pits placed from rim to rim. Panel **(b)** depicts the FeS melt texture observed for run ESS-V140A-FeS, conducted at 1673 K, vacuum (0.0002 bar) for 15 min. This texture was found to be typical for experimental samples that experienced significant S loss, resulting in the separation of FeS-rich (dark) and FeS-poor (white) melts. Panel **(c)** shows an example of a typical Fe metal run product and panel **(d)** quench textures observed in the Fe melt of run ESS-1-150D-Fe.

external reference material for both high-pressure synthesized starting materials and all experimental run products (Jochum et al., 2005). The use of the ratio between the high *P-T* Fe or FeS reference material and experimental run products thus rules out any potential matrix effects from using the NIST-610 glass to obtain elemental concentrations (Steenstra et al., 2023). The Fe contents (assuming ^{56}Fe) of metal and sulfide samples, as measured by electron microprobe, were used as internal standards in all measurements. All LA-ICP-MS data was reduced using GLITTER software (van Achterbergh et al., 2001, Griffin et al., 2008). This also included monitoring and/or identification of heterogeneities or potential spatial compositional variations in the exposed section through the run products.

3. Results

3.1. Run products and homogeneity

Run products typically consisted of a single quenched metal or sulfide (Fig. 1), with textures that were like those observed in our previous study (Steenstra et al., 2023). All FeS samples showed textures that are typical for a liquid state of the FeS melt, in agreement with phase diagram predictions (Buono and Walker, 2011) (Fig. 1a,b). No evidence of specific exsolution of trace metals was found in either the metal or sulfide liquid. On the other hand, EPMA totals of the lower temperature Fe metal experiments performed at 1 bar indicate relative low C contents (<2 wt% C). This implies that the Fe samples in these experiments were only partially molten, yielding a much lower solubility limit of C (e.g., Yang et al., 2019). Although the eutectic temperature of C-saturated Fe

alloy is approximately 1420 K at 1 bar, the liquidus of C-free Fe alloy is much higher (1800 K; Buono and Walker, 2011). The lack of complete melting of several lower-temperature experiments at 1 bar can thus be explained by a combination of the heating times required for melting of the powdered starting materials and the time required for complete C saturation of the Fe sample by the surrounding graphite capsule.

The analyses indicate that the sulfide liquids suffered significant evaporative loss of S under vacuum, up to 82 %, leading to the formation of immiscible liquids, i.e., a S-poor, C-rich Fe melt and a S-rich, C-poor FeS melt on a relatively small scale (i.e., 20–50 μm; Fig. 1b, Table S2; Corgne et al., 2008; Steenstra et al., 2023). The use of 20–25 μm laser spot sizes, in conjunction with placing a large number of spots in grids, is expected to be sufficient for obtaining a representative bulk composition of the experiment (Table S1). Steenstra et al. (2023) showed that the concentrations of volatiles S, Cu, Ge, Ag were relatively constant throughout each sample. This suggests that redistribution of these elements, for example through rapid physical transport because of low viscosities, exceeds the rate of evaporation. Rim-to-rim lines and rasters of LA-ICP-MS spots obtained in this study generally do not show significant variation of the (highly) volatile elements (Fig. 2), consistent with our previous work (Steenstra et al., 2023).

Finally, post-experimental results showed that Fe experiments that were conducted simultaneously with FeS samples at 1 bar suffered from cross-contamination of S, despite a significant sample-to-sample distance of 0.5–1 cm and isolation of each sample in tall graphite buckets (Fig. S1). The degree of contamination increased strongly with temperature, with an increase from 0.12 ± 0.11 (1SD) wt.% S at 1673 K and 1 bar to 0.75 ± 0.08 (2SE) wt.% S at 1773 K and 1 bar. Sulfur cross-

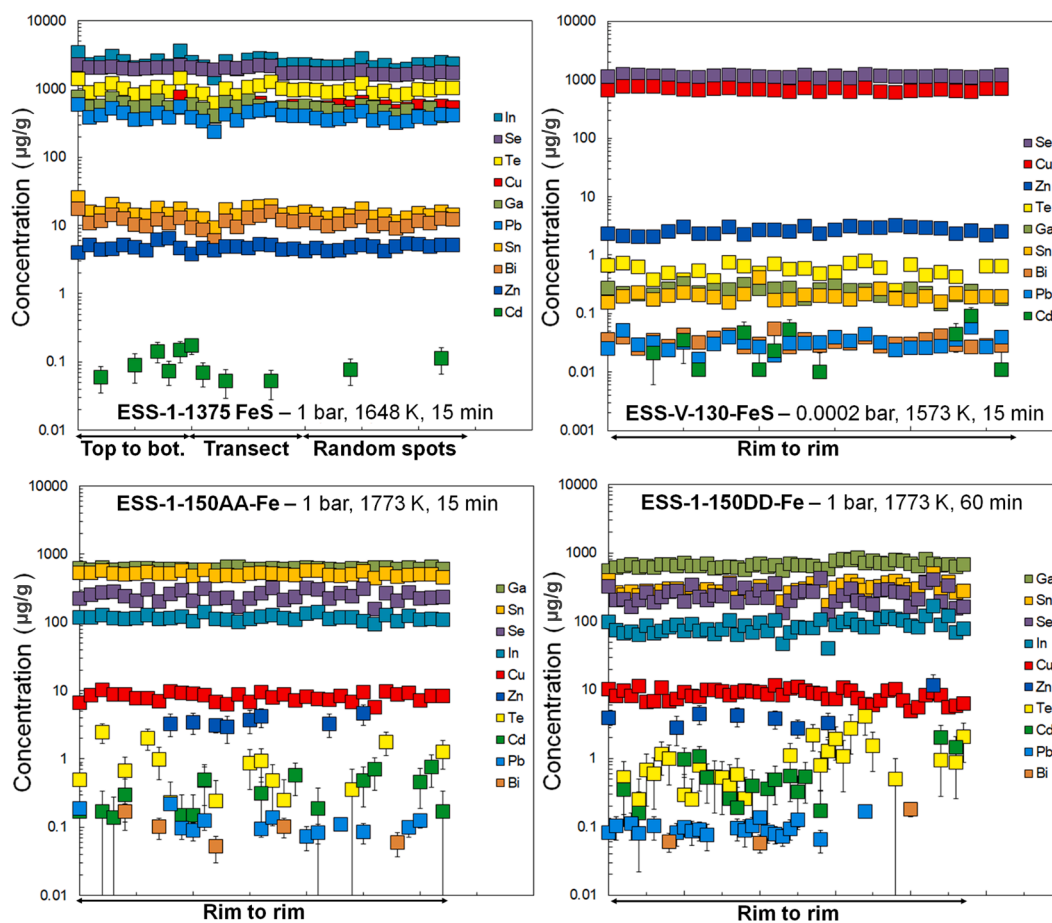**Fig. 2.** Concentration profiles for Cu, Zn, Ga, Se, Cd, In, Sn, Sb, Pb and Bi along rim-to-rim and/or vertical LA-ICP-MS spot transects in experimental samples ESS-1-1375 FeS, ESS-V-130-FeS, ESS-1-150AA-Fe and ESS-1-150DD-Fe. The measurements imply the lack of systematic variability of elemental concentrations throughout the samples. Uncertainties on individual spots are smaller than symbol sizes in most cases.

contamination was negligible under vacuum independent of experimental set-up and/or for experiments where only Fe samples were used (Fig. S1).

3.2. Elemental evaporation

3.2.1. Quantification of evaporative loss

The degree of evaporative loss of element i was calculated following the approach of Steenstra et al. (2023), or Eq. (1), which is the ratio between the concentration of element i in the experimental sample and the concentration of element i in the undegassed, high P-T synthesized reference material:

Evaporative loss factor of element $i \left(f^i \right)$

$$= \frac{\text{concentration of element } i \text{ in experimental sample (µg/g)}}{\text{concentration of element } i \text{ in reference material (µg/g)}} \quad (1)$$

The evaporative loss factors from Eq. (1) were normalized to Ni, which is not volatile within the explored experimental range:

$$\text{Ni} - \text{normalized evaporative loss factor of element i } f^{(i/\text{Ni})} = \frac{f^i}{f^{\text{Ni}}} \quad (2)$$

The effects of temperature (T) and time (t) on log $f^{(i/\text{Ni})}$ at a given pressure (0.0002 versus 1 bar) and composition (Fe versus FeS) were derived by parameterization of the data to Eq. (3) (Steenstra et al., 2023) using the ''multiple linear regression'' function of the Regress It© software:

$$\log f^{(i/\text{Ni})} = A + 1/T(\text{K}) + \log(\text{time}_{(\text{min})}) \quad (3)$$

Fit parameters were deemed statistically significant if $p < 0.10$. Table 2 shows the results.

It was found that several parameterizations obtained using Eq. (3) (significantly) underestimate the degree of evaporative loss (i.e., >0) at an experimental run time of t = 0. As observed in previous silicate and metallic melt evaporation studies (Sossi et al., 2019; Steenstra et al., 2023), the experimental run time does not necessarily correspond to the actual time of evaporation. This offset arises from the required time to (fully) melt the sample, which in turn depends on the experimental arrangement, sample (grain) size, thermal conductivity of the sample and/or powder composition. Thus, an incorporation of a lag time factor is required. The lag time factor (t_d) was thus defined by Eq. (4):

Effective degassing time (t_d in min)

$$= \text{experimental run time}(t \text{ in min}) - \text{lag time}(t_0 \text{ in min}) \quad (4)$$

where the actual experimental run time minus the lag time is defined as the ''effective degassing time'' or t_d (Sossi et al., 2019; Steenstra et al., 2023). As in the latter study, the lag time was determined for each element (where applicable) by using the difference between the modeled log $f^{(i/\text{Ni})}$ value and 0 at the start of the experiment (experimental run time t = 0 min) at the temperature of interest. The lag time also varies with temperature and an exponential fit was considered to this effect, where possible (Table 2). At 1673–1773 K the derived lag times range from zero to 15–20 min, depending on the element and temperature, which could in turn be related to variable diffusion rates of the elements of interest. The magnitude overall agrees with previously reported values for other elements from both metallic (Steenstra et al., 2023) and silicate melts (Sossi et al., 2019). For some elements (i.e., Se, In, Sn) in the Fe samples, the parameterization of data obtained throughout the explored temperature range at a given pressure returned negative effects of temperature on evaporation rates. As this seems physically impossible, the data for these elements was also separately fitted at a constant temperature, involving only experimental run time as a free parameter (Table 2). This yielded more realistic fitting results

(Table 2).

For comparison purposes, we also calculated the reaction rate constants or k_i values of the evaporation of Zn, Ga, Se, Cd, In, Sn, Sb, Te, Pb, Bi from Fe and/or FeS melt using the latter kinetic approach. The k_i values can be derived from the relation of the natural logarithm of the ratio with the initial concentration (C_0) and the post-experimentally measured concentration (C):

$$\ln(\text{C/C}_0) = -\frac{3k_it}{r} \quad (5)$$

where r is the radius of the sample in cm and t is the time in minutes (Tsuchiyama et al., 1981; Sossi et al., 2019, Steenstra et al., 2023; Flemetakis et al., 2024). The parameter r was fixed to 0.15 cm (Steenstra et al., 2023) and slopes of ln(C/ C_0) versus time were derived at a given set of pressure and temperature conditions. Rearranging of Eq. (5) yields Eq. (6), with which the k_i values can be obtained:

$$k_i = \frac{\text{slope*r}}{-3} \quad (6)$$

The k_i values of the elements of interest are listed in Table 3. It should be noted that the highly volatile elements (e.g., Zn, Te, In, Sn, Cd, Bi) extensively evaporated, with the degree depending on the experimental P-T conditions and composition. As a result, their concentrations were close to or below LA-ICP-MS detection limits in several instances. Some of the derived k_i values therefore represent lower limits (c.f., Table 3). Finally, some Fe experiments conducted at 1 bar, at relatively low temperatures (<1673 K) and for relatively short run durations (usually <15 min) were not fully liquid at peak temperature (Table 1, Supplementary Material). This could affect the degree of evaporation of the elements of interest from these samples. However, the well-established relations between evaporative loss factors and time for volatile elements such as Te, In and Sn implies that a (partially) solid state of the metal did not significantly affect the extent and rate of evaporation of the elements considered in this work (Fig. 3, Tables 2,3).

3.2.2. Fe experiments

The Fe metal run products experienced significant evaporative loss of In, Cd, Sn, Te, Pb, Bi, at 1 bar and 1573–1773 K, but not of Ga, Se and Sb (Table S1). Decreasing the pressure from 1 to 0.0002 bar yields evaporative loss for all elements considered, in a volatility sequence of Se < Te, Ga, Sb, In < Zn, Sn, Cd, Pb, Bi. It should be noted that many of the latter elements are so rapidly evaporated that concentrations are commonly close to or below detection limit of LA-ICP-MS, prohibiting an accurate assessment of the relative volatilities of most notably Zn, Cd, Pb and Bi. Consideration of the post-experimentally measured Ni contents for Fe samples confirmed the non-volatile behavior of Ni, yielding an average ln(C/C$_0$) value of –0.04 ± 0.03 (2SE) for all Fe experiments (N=44). The derived parameterizations describing their evaporative loss factors as a function of temperature and time and reaction rate constant (k_i) values are listed in Tables 2 and 3, respectively.

3.2.3. FeS experiments

Geochemical analyses of the FeS samples showed extensive evaporation of virtually all elements considered, except for S and Se, at 1 bar and 1573–1773 K, with a volatility sequence of In, Ga < Sb, Te < Pb, Sn, Bi < Zn < Cd. Evaporation of Cd, and to a lesser extent Zn, occurs very fast, yielding post-experimentally measured concentrations that are close to or even below LA-ICP-MS detection limits in most experiments (Table S2). As predicted from thermodynamic considerations, decreasing the pressure from 1 to 0.0002 bar additionally increases the volatility of all elements considered, with S and Se also being extensively lost through evaporation. Nickel is not volatile, independent of the pressure and temperature explored here, with an average ln(C/C$_0$) value of –0.07 ± 0.06 (2SE) for all FeS experiments (N = 41). A summary of the evaporative loss factor parameterizations and (k_i) values for FeS

Table 2
Parameterizations describing elemental volatility for FeS and Fe liquids.

Log	P (bar)	A	B (1/T in K)	C log (exp. run time t in min)	N	R²	Lag time t₀ in min	Comment
S/Ni (FeS) [1]	0.0010	−1.286(1093)	3310(1874)	−0.725(116)	11	0.83	$7701e^{-0.00402053 * T(K)}$	–
S/Ni (FeS) [2]	0.0002–0.0010	−4.601(2042)	9062(3447)	−0.868(223)	21	0.53	$1.256 \times 10^8 e^{-0.00982223 * T(K)}$	All data, including from ref. (1)
Cu/Ni (FeS) [**]	0.0010	1.496(4820)	n.s.s. [a]	−1.498(354)	10	0.69	10	–
Cu/Ni (Fe) [**]	0.0010	−9.912(1507)	19855(2397)	−2.245(164)	14	0.97	$5032367e^{-0.00801547 * T(K)}$	–
Zn/Ni (Fe)	0.0002	No fit possible	–	–	13	–	–	All data
Zn/Ni (Fe)	1	No fit possible	–	–	32	–	–	All data
Zn/Ni (FeS) [**]	0.0002	−2.204(107)	n.s.s.	−0.217(85)	9	0.48	–	All data
Zn/Ni (FeS)[*]	1	−10.121(2454)	16024(4232)	−1.010(230)	32	0.51	–	All data
Ga/Ni (Fe) [*, **]	0.0002	−19.417(3497)	34069(5897)	−1.791(466)	13	0.82	$8.954 \times 10^{12} e^{-0.01693978 * T(K)}$	All data
Ga/Ni (FeS) [**]	0.0002	No fit possible	–	–	9	–	–	All data
Ga/Ni (FeS) [*]	1	−2.046(576)	3463(994)	−0.183(54)	32	0.42	–	All data
Ga/Ni (FeS)	1	−2.675(844)	4537(1447)	−0.201(73)	20	0.49	$3.581 \times 10^{15} e^{-0.02108190 * T(K)}$	Indiv. experim. only
Se/Ni (Fe) [**]	0.0002	No fit possible	–	–	12	–	–	All data
Se/Ni (Fe)	1	1.317(236)	n.s.s.	−0.935(182)	32	0.47	25	All data
Se/Ni (Fe)	1	3.408(1381)	−4590(2408)	−0.367(150)	12	0.56		S-cont. data only
Se/Ni (Fe) [*]	1	1.536(299)	n.s.s.	−1.181(231)	20	0.59	20	S-cont. data excl.
Se/Ni (FeS [*, **]	0.0002	−14.039(7882)	26543(13701)	−1.832(980)	9	0.48	$2.928 \times 10^9 e^{-0.01291417 * T(K)}$	All data
Cd/Ni (Fe)	0.0002	No fit possible	–	–	12	–	–	All data
Cd/Ni (Fe)	1	No fit possible	–	–	31	–	–	All data
Cd/Ni (FeS)	0.0002	No fit possible	–	–	8	–	–	All data
Cd/Ni (FeS)[*]	1	−4.041(226)	n.s.s.	−0.341(170)	32	0.12	–	All data
In/Ni (Fe) [**]	0.0002	−2.663(374)	n.s.s.	−0.495(288)	13	0.21	–	All data
In/Ni (Fe)	1	11.471(3747)	−19540(6531)	−0.876(361)	32	0.38	–	All data
In/Ni (Fe)	1	11.310(3665)	−18123(3665)	−0.861(228)	12	0.84	–	S-cont. data only
In/Ni (Fe) [*]	1	11.549(3192)	−20173(5562)	−0.972(289)	20	0.63	–	S-cont. data excl.
In/Ni (Fe)	1	−0.463(777)	Not fitted	−1.005(524)	6	0.48	–	S-cont. data excl., 1673 K only
In/Ni (Fe)	1	0.122(373)	Not fitted	−0.908(306)	9	0.56	1.3	S-cont. data excl., 1773 K only
In/Ni (FeS) [**]	0.0002	−8.485(2224)	10036(3866)	−1.288(276)	9	0.79	–	All data
In/Ni (FeS) [*]	1	−2.334(775)	4037(1336)	−0.216(73)	32	0.36	$15.90 \times 10^{13} e^{-0.01760841* T(K)}$	All data
Sn/Ni (Fe) [**]	0.0002	−7.456(1750)	7454(2951)	−0.359(233)	13	0.46	–	All data
Sn/Ni (Fe)	1	11.883(3888)	−18123(3665)	−0.861(228)	32	0.52	–	All data
Sn/Ni (Fe)	1	8.204(1578)	−12977(2752)	−0.815(171)	12	0.86	–	S-cont. data only
Sn/Ni (Fe) [*]	1	14.090(3404)	−22261(5931)	−2.033(308)	20	0.80	2.3 at 1673 K	S-cont. data excl.
Sn/Ni (Fe)	1	1.007(457)	Not fitted	−2.295(308)	6	0.93	2.7	S-cont. data excl., 1673 K only
Sn/Ni (Fe)	1	0.679(452)	Not fitted	−1.260(371)	9	0.62	3.5	S-cont. data excl., 1773 K only
Sn/Ni (FeS) [**]	0.0002	−6.331(1014)	3703(1763)	−0.289(126)	9	0.55	–	All data
Sn/Ni (FeS) [*]	1	−15.324(4879)	26928(8415)	−2.604(458)	32	0.57	$2.548 \times 10^7 e^{-0.00975385 * T(K)}$	All data
Sb/Ni (Fe) [*, **]	0.0002	−20.873(4658)	32816(7854)	−0.888(621)	13	0.66	$7.291 \times 10^{26} e^{-0.03940371 * T(K)}$	All data
Sb/Ni (Fe)	1	No fit possible	–	–	32	–	–	All data
Sb/Ni (Fe)	1	No fit possible	–	–	12	–	–	S-cont. data only
Sb/Ni (Fe)	1	No fit possible	–	–	20	–	–	S-cont. data excluded
Sb/Ni (FeS) [**]	0.0002	No fit possible	–	–	9	–	–	All data
Sb/Ni (FeS) [*]	1	−2.898(436)	4799(751)	−0.461(41)	32	0.84	$1.321 \times 10^7 e^{-0.00985765 * T(K)}$	All data
Te/Ni (Fe) [**]	0.0002	No fit possible	–	–	13	–	–	All data
Te/Ni (Fe)	1	No fit possible	–	–	32	–	–	All data
Te/Ni (Fe) [*]	1	−3.821(2044)	7517(3564)	−1.322(222)	12	0.80	$19228e^{-0.00511788 * T(K)}$	S-cont. data only
Te/Ni (Fe)	1	−9.451(2926)	13055(5098)	−0.594(265)	20	0.37	–	S-cont. data excluded
Te/Ni (FeS) [**]	0.0002	−3.283(270)	–	−0.451(216)	9	0.39	–	All data
Te/Ni (FeS)	1	−2.144(823)	3433(1420)	−0.448(77)	32	0.56	$200061e^{-0.00761275 * T(K)}$	All data
Pb/Ni (Fe) [**]	0.0002	No fit possible	–	–	13	–	–	All data

Table 2 (*continued*)

Log	P (bar)	A	B (1/T in K)	C log (exp. run time t in min)	N	R^2	Lag time t_0 in min	Comment
Pb/Ni (Fe)	1	−11.312(2734)	16502(4732)	−0.836(289)	31	0.40	−	All data
Pb/Ni (Fe) *	1	−7.348(2259)	11468(3940)	−1.352(245)	12	0.79	$594693e^{−0.00848240 * T(K)}$	S-cont. data only
Pb/Ni (Fe)	1	−13.699(2866)	19883(4937)	−0.683(300)	19	0.56	−	S-cont. data excluded
Pb/Ni (FeS) **	0.0002	No fit possible	−	−	12	−	−	All data
Pb/Ni (FeS) *	1	−16.363(3488)	31441(6015)	−3.135(328)	32	0.79	$4.466 × 10^7 e^{−0.009443152 * T(K)}$	All data
Bi/Ni (Fe) **	0.0002	No fit possible	−	−	13	−	−	All data
Bi/Ni (Fe)	1	−17.244(2489)	25867(4338)	−1.039(289)	32	0.62	$2.702 × 10^{18} e^{−0.02833505 * T(K)}$	All data
Bi/Ni (Fe)	1	−13.198(2477)	20512(4320)	−1.551(269)	12	0.84	$3.154 × 10^9 e^{−0.01407337 * T(K)}$	S-cont. data only
Bi/Ni (Fe)	1	−19.739(2913)	29483(5076)	−0.859(264)	20	0.70	$2.048 × 10^{25} e^{−0.03906292 * T(K)}$	S-cont. data excluded
Bi/Ni (FeS) **	0.0002	No fit possible	−	−	12	−	−	All data
Bi/Ni (FeS) *	1	−17.096(3965)	30573(6839)	−3.306(372)	32	0.76	$5219453e^{−0.008872650 * T(K)}$	All data

* Parameterizations marked with asterisk were used for modeling trend lines in Figs. 3 and 4.

** Parameterizations marked with two asterisks were used for modeling the expected depletions in magmatic iron meteorite parent bodies (Fig. 8).

[a] n.s.s. = not statistically significant at $p = 0.15$ [b] due to high volatility samples were (almost) fully degassed at any pressure, temperature and time considered [1] Parameterization from Steenstra et al. (2023) [2] Fitted using data from this study and the study of Steenstra et al. (2023).

melts are shown in Tables 2 and 3.

3.2.4. Effects of metal composition on volatility

The composition of the melt that is exposed to evaporation as well as the composition of the gas itself can strongly affect the volatility of the elements of interest (e.g., Renggli and Klemme, 2020). This is due to the variation in the activities of components in the melt with variable melt composition, yielding a particular equilibrium partial pressure for the species in the vapor that controls their evaporation rate (e.g., Ivanova et al., 2021). In terms of metallic melts, the results of Steenstra et al. (2023) indicate very strong effects of S in the metallic melt on the volatility of most notably Ge and Ag. Ge and Mo, nominally chalcophobic or sulfide–avoiding elements, are significantly more volatile in S-rich melts compared to S-poor or S-free metal liquids, due to their much higher activity coefficients in FeS melt relative to Fe liquid (Wood et al., 2014). Of the other elements considered in Wood et al. (2014) which are studied here, Ga and Sb also have higher activity coefficients in FeS melt compared to Fe liquid, and these elements are indeed observed to be more volatile in FeS melt relative to Fe liquid (Figs. 3, 4, Tables 2,3).

On the other hand, we have shown that chalcophiles Ag and Cu are significantly less volatile in S-rich melt compared to S-poor metal liquids (Steenstra et al., 2023), a direct result of their very low activity co-efficients in FeS melt, compared to Fe liquid (Wood et al., 2014; 2019). Indeed, chalcophiles In, Sn, Te, Pb and Bi are also observed to evaporate significantly more from Fe liquid relative to FeS melt at a given pressure, temperature and time (Figs. 3, 4; Tables 2,3). The relatively strong effects of S on the volatility of other elements are also evident from their anomalous behavior in the S-contaminated Fe metal runs, which yield lower-than-expected evaporative loss factors for In, Sn, Te, Pb and Bi relative to nominally S-free Fe metal experiments (Fig. 3; Tables 2,3).

It should be noted that besides metal composition, oxygen fugacity may also affect elemental evaporation. For example, the evaporation behavior of Te from silicate melts was experimentally constrained by Renggli et al. (2022) and they found that the volatility of Te is increased with increasing oxygen fugacity, presumably a result of Te being dissolved as $Te^{2−}$ and replacing $O^{2−}$ in the silicate melt structure. Although the oxygen fugacities of the experiments of this study did not vary significantly due to buffering of the sample by the graphite bucket and/or by CO gas, volatility would not be affected directly by changes in oxygen fugacity, as speciation within the FeS and/or Fe melt is not expected to change. Oxygen fugacity could also result in different gas phase speciation of the elements of interest (Sossi et al., 2019; Renggli et al., 2022), which in turn could affect elemental volatilities. For some elements, variable oxygen fugacity does not seem to yield significant differences in its gas speciation (e.g., Te; Renggli et al., 2022), but for other elements this is likely more important (Norris and Wood, 2017).

Altogether, these results confirm the key role of the composition of the medium from which the elements of interest evaporate, especially for elemental evaporation from metal melts. This also implies that the high activity coefficients of virtually all of the siderophile, chalcophile and lithophile elements of interest in highly reduced, Si-bearing Fe liquid yields significantly more volatile behavior of all of the latter elements, relative to Fe melt (Tuff et al., 2011; Righter et al., 2018; Steenstra et al., 2020a). This should be confirmed and quantitatively constrained in future experimental work.

4. Discussion

4.1. Revised volatility sequences

Combining the new results with the work of Steenstra et al. (2023) allows for building of models that can be used to predict the volatility of most volatile metals. The condensation temperature models (Lodders, 2003; Wood et al., 2019) suggests a sequence of the 50 % condensation temperature applicable to a solar gas composition at $10^{−4}$ bar ($T_{50\%}$) = Bi, In, Pb, Cd < Sn < Te, S<Ag, Se, Zn < Ge < Sb < Ga < Cu. The results

Table 3

Calculated ki values (reaction rate constants; Eq. (5) obtained for each element at a given set of temperature and pressure conditions. The y-axis intercept was forced to 0 with slope determination. All calculations were conducted assuming a radius of 0.15 cm (Steenstra et al., 2023). Asterisks indicate a minimum reaction rate as evaporation occurred until LA-ICP-MS detection limits were reached (see main text for details).

	Comp.	T (K)	Pressure	Time range (min)	k_i (cm/min)	Slope	1SE	R^2	N	Comment
S	FeS	1773	1 bar	5–120	6.00×10^{-5}	-1.20×10^{-3}	3.00×10^{-4}	0.78	6	From Steenstra et al. (2023)
S	FeS	1673	vacuum	15–120	9.80×10^{-4}	-1.95×10^{-2}	1.80×10^{-3}	0.97	5	From Steenstra et al. (2023)
S	FeS	1773	vacuum	5–60	3.66×10^{-3}	-7.31×10^{-2}	8.90×10^{-3}	0.97	3	From Steenstra et al. (2023)
S	FeS	1673	1 bar	15–60	4.29×10^{-5}	-8.60×10^{-4}	4.17×10^{-4}	0.68	3	Data obtained together with Fe-rich samples
S	FeS	1673	1 bar	5–120	3.92×10^{-5}	-7.84×10^{-4}	1.37×10^{-4}	0.82	8	Data obtained for FeS-rich samples only
S	FeS	1773	1 bar	5–60	7.71×10^{-5}	-1.54×10^{-3}	6.42×10^{-4}	0.59	5	Data obtained together with Fe-rich samples
S	FeS	1773	1 bar	5–60	8.68×10^{-5}	-1.74×10^{-3}	4.25×10^{-4}	0.70	8	Data obtained for FeS-rich samples only
S	FeS	1673	vacuum	15–60	7.90×10^{-4}	-1.58×10^{-2}	5.33×10^{-3}	0.81	3	Data obtained for FeS-rich samples only
Zn*	FeS	1673	1 bar	15–60	$>6.11 \times 10^{-3}$	-1.22×10^{-1}	3.55×10^{-2}	0.86	3	Data obtained together with Fe-rich samples
Zn*	FeS	1673	1 bar	5–120	$>3.80 \times 10^{-3}$	-7.60×10^{-2}	2.23×10^{-2}	0.62	8	Data obtained for FeS-rich samples only
Zn*	FeS	1673	1 bar	5–60	$>6.75 \times 10^{-3}$	-1.35×10^{-1}	2.88×10^{-2}	0.79	7	Data obtained for FeS-rich samples only; removed 120 min exp
Zn*	FeS	1773	1 bar	5–60	$>7.14 \times 10^{-3}$	-1.43×10^{-1}	4.42×10^{-2}	0.72	5	Data obtained together with Fe-rich samples
Zn*	FeS	1773	1 bar	5–60	$>7.32 \times 10^{-3}$	-1.46×10^{-1}	3.74×10^{-2}	0.69	8	Data obtained for FeS-rich samples only
Zn*	FeS	1673	vacuum	15–60	$>6.24 \times 10^{-3}$	-1.25×10^{-1}	4.64×10^{-2}	0.78	3	Data obtained for FeS-rich samples only
Zn*	FeS	1673	vacuum	15–30	$>1.11 \times 10^{-2}$	-2.22×10^{-1}	7.59×10^{-2}	0.90	2	Data obtained for FeS-rich samples only; removed 60 min exp
Zn*	Fe	1673	1 bar	15–60	$>5.51 \times 10^{-3}$	-1.10×10^{-1}	4.02×10^{-2}	0.79	3	Data obtained together with FeS-rich samples
Zn*	Fe	1673	1 bar	5–120	$>2.65 \times 10^{-3}$	-5.29×10^{-2}	2.45×10^{-2}	0.48	6	Data obtained for Fe-rich samples only
Zn*	Fe	1773	1 bar	5–60	$>6.62 \times 10^{-3}$	-1.32×10^{-1}	5.33×10^{-2}	0.61	3	Data obtained together with FeS-rich samples
Zn*	Fe	1773	1 bar	5–30	$>1.33 \times 10^{-2}$	-2.65×10^{-1}	6.92×10^{-2}	0.75	6	Data obtained for Fe-rich samples only
Zn*	Fe	1673	vacuum	15–60	$>5.17 \times 10^{-3}$	-1.03×10^{-1}	4.45×10^{-2}	0.73	3	Data obtained for Fe-rich samples only
Zn*	Fe	1773	vacuum	5–60	$>4.80 \times 10^{-3}$	-9.59×10^{-2}	4.42×10^{-2}	0.54	5	Data obtained for Fe-rich samples only
Ga	FeS	1673	1 bar	15–60	6.03×10^{-4}	-1.21×10^{-2}	3.74×10^{-3}	0.84	3	Data obtained together with Fe-rich samples
Ga	FeS	1673	1 bar	5–120	6.41×10^{-4}	$-1.28 \times \times 10^{-2}$	3.68×10^{-3}	0.63	8	Data obtained for FeS-rich samples only
Ga	FeS	1773	1 bar	5–60	7.64×10^{-4}	-1.53×10^{-2}	4.86×10^{-3}	0.71	5	Data obtained together with Fe-rich samples
Ga	FeS	1773	1 bar	5–60	1.51×10^{-3}	-3.02×10^{-2}	6.42×10^{-3}	0.76	8	Data obtained for FeS-rich samples only
Ga	FeS	1673	vacuum	15–60	8.16×10^{-3}	-1.63×10^{-1}	5.43×10^{-2}	0.82	3	Data obtained for FeS-rich samples only
Ga	FeS	1673	vacuum	15–30	1.46×10^{-2}	-2.91×10^{-1}	5.70×10^{-2}	0.96	2	Data obtained for FeS-rich samples only; removed 60 min exp
Ga	Fe	1673–1773	1 bar	5–120	*non-volatile*	–	–	–	–	–
Ga	Fe	1673	vacuum	15–60	5.18×10^{-3}	-1.04×10^{-1}	1.00×10^{-2}	0.98	3	Data obtained for Fe-rich samples only
Ga	Fe	1773	vacuum	5–60	7.41×10^{-3}	-1.48×10^{-1}	4.52×10^{-2}	0.73	5	Data obtained for Fe-rich samples only
Se	FeS	1673–1773	1 bar	5–120	*non-volatile*	–	–	–	–	–
Se	FeS	1673	vacuum	15–60	2.38×10^{-3}	-4.77×10^{-2}	1.42×10^{-2}	0.85	3	Data obtained for FeS-rich samples only
Se	Fe	1673–1773	1 bar	5–120	*non-volatile*	–	–	–	–	–
Se*	Fe	1673	vacuum	15–60	$>2.38 \times 10^{-3}$	-4.75×10^{-2}	3.19×10^{-2}	0.69	2	Data obtained for Fe-rich samples only
Se*	Fe	1773	vacuum	5–60	$>2.79 \times 10^{-3}$	-5.56×10^{-2}	2.25×10^{-2}	0.60	5	Data obtained for Fe-rich samples only
Te	FeS	1673	1 bar	15–60	1.64×10^{-3}	-3.27×10^{-2}	9.12×10^{-3}	0.87	3	Data obtained together with Fe-rich samples
Te	FeS	1673	1 bar	5–120	1.74×10^{-3}	-3.49×10^{-2}	7.62×10^{-3}	0.75	8	Data obtained for FeS-rich samples only

Table 3 (*continued*)

	Comp.	T (K)	Pressure	Time range (min)	k_i (cm/min)	Slope	1SE	R^2	N	Comment
Te	FeS	1773	1 bar	5–60	2.05×10^{-3}	-4.10×10^{-2}	1.26×10^{-2}	0.73	5	Data obtained together with Fe-rich samples
Te	FeS	1773	1 bar	5–60	3.22×10^{-3}	-6.45×10^{-2}	1.23×10^{-2}	0.80	8	Data obtained for FeS-rich samples only
Te	FeS	1673	vacuum	15–60	9.82×10^{-3}	-1.96×10^{-1}	6.39×10^{-2}	0.83	3	Data obtained for FeS-rich samples only
Te	FeS	1673	vacuum	15–30	1.68×10^{-2}	-3.37×10^{-1}	9.17×10^{-2}	0.93	2	Data obtained for FeS-rich samples only; removed 60 min exp
Te	Fe	1673	1 bar	15–60	3.84×10^{-3}	-7.68×10^{-2}	1.47×10^{-2}	0.93	3	Data obtained together with FeS-rich samples
Te	Fe	1673	1 bar	5–120	3.50×10^{-3}	-7.00×10^{-2}	2.75×10^{-2}	0.56	6	Data obtained for Fe-rich samples only
Te	Fe	1773	1 bar	5–60	4.40×10^{-3}	-8.80×10^{-2}	1.86×10^{-2}	0.85	5	Data obtained together with FeS-rich samples
Te	Fe	1773	1 bar	5–60	9.36×10^{-3}	-1.87×10^{-1}	5.86×10^{-2}	0.59	8	Data obtained for Fe-rich samples only
Te*	Fe	1673	vacuum	15–60	$>7.72 \times 10^{-3}$	-1.54×10^{-1}	6.45×10^{-2}	0.74	3	Data obtained for Fe-rich samples only
Te*	Fe	1773	vacuum	5–60	$>8.01 \times 10^{-3}$	-1.60×10^{-1}	6.30×10^{-2}	0.62	5	Data obtained for Fe-rich samples only
Cd*	FeS	1673	1 bar	15–60	$>1.36 \times 10^{-2}$	-2.35×10^{-1}	8.97×10^{-2}	0.78	3	Data obtained together with Fe-rich samples
Cd*	FeS	1673	1 bar	5–120	$>1.18 \times 10^{-2}$	-1.51×10^{-1}	4.86×10^{-2}	0.58	8	Data obtained for FeS-rich samples only
Cd*	FeS	1773	1 bar	5–60	$>1.29 \times 10^{-2}$	-2.58×10^{-1}	1.07×10^{-1}	0.60	5	Data obtained together with Fe-rich samples
Cd*	FeS	1773	1 bar	5–60	$>1.38 \times 10^{-2}$	-2.76×10^{-1}	7.57×10^{-2}	0.65	8	Data obtained for FeS-rich samples only
Cd*	FeS	1673	vacuum	15–60	$>1.11 \times 10^{-2}$	-2.22×10^{-1}	8.88×10^{-2}	0.76	3	Data obtained for FeS-rich samples only
Cd*	FeS	1673	vacuum	15–30	$>2.07 \times 10^{-2}$	-4.14×10^{-1}	1.34×10^{-1}	0.91	2	Data obtained for FeS-rich samples only; removed 60 min exp
Cd*	Fe	1673	1 bar	15–60	$>7.17 \times 10^{-3}$	-1.43×10^{-1}	5.93×10^{-2}	0.75	3	Data obtained together with FeS-rich samples
Cd*	Fe	1673	1 bar	5–120	$>3.50 \times 10^{-3}$	-7.01×10^{-2}	2.97×10^{-2}	0.53	6	Data obtained for Fe-rich samples only
Cd*	Fe	1773	1 bar	5–60	$>8.23 \times 10^{-3}$	-1.65×10^{-1}	6.98×10^{-2}	0.58	5	Data obtained together with FeS-rich samples
Cd*	Fe	1773	1 bar	5–60	$>8.25 \times 10^{-3}$	-1.65×10^{-1}	6.32×10^{-2}	0.49	8	Data obtained for Fe-rich samples only
Cd*	Fe	1673	vacuum	15–60	$>6.35 \times 10^{-3}$	-1.27×10^{-1}	5.96×10^{-2}	0.69	3	Data obtained for Fe-rich samples only
Cd*	Fe	1773	vacuum	5–60	$>6.57 \times 10^{-3}$	-1.31×10^{-1}	5.64×10^{-2}	0.58	5	Data obtained for Fe-rich samples only
In	FeS	1673	1 bar	15–60	4.32×10^{-4}	-8.64×10^{-3}	2.29×10^{-3}	0.88	3	Data obtained together with Fe-rich samples
In	FeS	1673	1 bar	5–120	6.40×10^{-4}	-1.28×10^{-2}	3.56×10^{-3}	0.65	8	Data obtained for FeS-rich samples only
In	FeS	1773	1 bar	5–60	6.48×10^{-4}	-1.30×10^{-2}	3.12×10^{-3}	0.81	5	Data obtained together with Fe-rich samples
In	FeS	1773	1 bar	5–60	1.85×10^{-3}	-3.71×10^{-2}	5.57×10^{-3}	0.86	8	Data obtained for FeS-rich samples only
In	FeS	1673	vacuum	15–60	1.08×10^{-2}	-2.17×10^{-2}	4.61×10^{-2}	0.92	3	Data obtained for FeS-rich samples only
In	FeS	1673	vacuum	15–30	1.65×10^{-2}	-3.30×10^{-1}	3.12×10^{-2}	0.99	2	Data obtained for FeS-rich samples only; removed 60 min exp
In	Fe	1673	1 bar	15–60	2.70×10^{-3}	-5.39×10^{-2}	1.06×10^{-2}	0.93	3	Data obtained together with FeS-rich samples
In	Fe	1673	1 bar	5–120	2.86×10^{-3}	-5.72×10^{-2}	2.10×10^{-2}	0.60	6	Data obtained for Fe-rich samples only
In	Fe	1773	1 bar	5–60	4.19×10^{-4}	-8.38×10^{-3}	9.78×10^{-3}	0.16	5	Data obtained together with FeS-rich samples
In	Fe	1773	1 bar	5–60	3.93×10^{-3}	-7.86×10^{-2}	1.47×10^{-2}	0.80	8	Data obtained for Fe-rich samples only
In*	Fe	1673	vacuum	15–60	$>8.80 \times 10^{-3}$	-1.76×10^{-1}	6.46×10^{-2}	0.79	3	Data obtained for Fe-rich samples only
In*	Fe	1773	vacuum	5–60	$>9.89 \times 10^{-3}$	-1.98×10^{-1}	7.41×10^{-2}	0.64	5	Data obtained for Fe-rich samples only
Sn	FeS	1673	1 bar	15–60	6.43×10^{-3}	-1.29×10^{-1}	2.54×10^{-2}	0.93	3	Data obtained together with Fe-rich samples
Sn	FeS	1673	1 bar	5–120	7.15×10^{-3}	-1.43×10^{-1}	2.68×10^{-2}	0.78	8	Data obtained for FeS-rich samples only
Sn	FeS	1773	1 bar	5–60	7.89×10^{-3}	-1.58×10^{-1}	5.08×10^{-2}	0.71	5	Data obtained together with Fe-rich samples

Table 3 (*continued*)

	Comp.	T (K)	Pressure	Time range (min)	k_i (cm/min)	Slope	1SE	R^2	N	Comment
Sn	FeS	1773	1 bar	5–60	1.39×10^{-2}	-2.78×10^{-1}	5.76×10^{-2}	0.77	8	Data obtained for FeS-rich samples only
Sn*	FeS	1673	vacuum	15–60	$>1.14 \times 10^{-2}$	-2.28×10^{-1}	7.37×10^{-2}	0.83	3	Data obtained for FeS-rich samples only
Sn*	FeS	1673	vacuum	15–30	$>1.99 \times 10^{-2}$	-3.97×10^{-1}	8.83×10^{-2}	0.95	2	Data obtained for FeS-rich samples only; removed 60 min exp
Sn	Fe	1673	1 bar	15–60	2.65×10^{-3}	-5.30×10^{-2}	6.82×10^{-3}	0.97	3	Data obtained together with FeS-rich samples
Sn	Fe	1673	1 bar	5–120	4.17×10^{-3}	-8.33×10^{-2}	1.76×10^{-2}	0.82	6	Data obtained for Fe-rich samples only
Sn	Fe	1773	1 bar	5–60	8.37×10^{-4}	-1.67×10^{-2}	5.96×10^{-3}	0.66	5	Data obtained together with FeS-rich samples
Sn	Fe	1773	1 bar	5–60	3.92×10^{-3}	-7.83×10^{-2}	9.93×10^{-3}	0.90	8	Data obtained for Fe-rich samples only
Sn*	Fe	1673	vacuum	15–60	$>9.87 \times 10^{-3}$	-1.97×10^{-1}	6.79×10^{-2}	0.81	3	Data obtained for Fe-rich samples only
Sn*	Fe	1773	vacuum	5–60	$>1.02 \times 10^{-2}$	-2.04×10^{-1}	8.38×10^{-2}	0.60	5	Data obtained for Fe-rich samples only
Sb	FeS	1673	1 bar	15–60	1.65×10^{-3}	-3.54×10^{-2}	1.24×10^{-2}	0.80	3	Data obtained together with Fe-rich samples
Sb	FeS	1673	1 bar	5–120	1.77×10^{-3}	-3.30×10^{-2}	6.13×10^{-3}	0.81	8	Data obtained for FeS-rich samples only
Sb	FeS	1773	1 bar	5–60	2.48×10^{-3}	-4.97×10^{-2}	1.41×10^{-2}	0.76	5	Data obtained together with Fe-rich samples
Sb	FeS	1773	1 bar	5–60	2.81×10^{-3}	-5.62×10^{-2}	1.15×10^{-1}	0.77	8	Data obtained for FeS-rich samples only
Sb	FeS	1673	vacuum	15–60	8.16×10^{-3}	-1.63×10^{-1}	4.73×10^{-2}	0.86	3	Data obtained for FeS-rich samples only
Sb	FeS	1673	vacuum	15–30	1.37×10^{-2}	-2.75×10^{-1}	5.04×10^{-2}	0.97	2	Data obtained for FeS-rich samples only; removed 60 min exp
Sb	Fe	1673–1773	1 bar	5–120	*non-volatile*	–	–	–	–	–
Sb	Fe	1673	vacuum	15–60	8.40×10^{-3}	-1.68×10^{-1}	3.67×10^{-2}	0.91	3	Data obtained for Fe-rich samples only
Sb	Fe	1773	vacuum	5–60	9.27×10^{-3}	-1.85×10^{-1}	7.69×10^{-2}	0.59	5	Data obtained for Fe-rich samples only
Pb	FeS	1673	1 bar	15–60	5.12×10^{-3}	-1.02×10^{-1}	9.87×10^{-3}	0.98	3	Data obtained together with Fe-rich samples
Pb	FeS	1673	1 bar	5–120	5.81×10^{-3}	-1.16×10^{-1}	1.07×10^{-2}	0.94	8	Data obtained for FeS-rich samples only
Pb	FeS	1773	1 bar	5–60	8.18×10^{-3}	-1.64×10^{-1}	1.53×10^{-2}	0.97	5	Data obtained together with Fe-rich samples
Pb	FeS	1773	1 bar	5–60	1.15×10^{-2}	-2.31×10^{-1}	3.74×10^{-2}	0.84	8	Data obtained for FeS-rich samples only
Pb	FeS	1673	vacuum	15–60	1.28×10^{-2}	-2.56×10^{-1}	8.83×10^{-2}	0.81	3	Data obtained for FeS-rich samples only
Pb	FeS	1673	vacuum	15–30	2.29×10^{-2}	-4.57×10^{-1}	1.11×10^{-1}	0.94	2	Data obtained for FeS-rich samples only; removed 60 min exp
Pb	Fe	1673	1 bar	15–60	$>7.23 \times 10^{-3}$	-1.45×10^{-1}	3.95×10^{-2}	0.87	3	Data obtained together with FeS-rich samples
Pb	Fe	1673	1 bar	5–90	$>6.04 \times 10^{-3}$	-1.21×10^{-1}	5.00×10^{-2}	0.59	5	Data obtained for Fe-rich samples only
Pb	Fe	1773	1 bar	5–60	$>8.13 \times 10^{-3}$	-1.63×10^{-1}	4.79×10^{-2}	0.74	5	Data obtained together with FeS-rich samples
Pb	Fe	1773	1 bar	5–60	$>1.11 \times 10^{-2}$	-2.21×10^{-1}	6.90×10^{-2}	0.60	8	Data obtained for Fe-rich samples only
Pb	Fe	1673	vacuum	15–60	$>6.91 \times 10^{-3}$	-1.38×10^{-1}	7.34×10^{-2}	0.64	3	Data obtained for Fe-rich samples only
Pb	Fe	1773	vacuum	5–60	$>8.77 \times 10^{-3}$	-1.75×10^{-1}	5.49×10^{-2}	0.72	5	Data obtained for Fe-rich samples only
Bi	FeS	1673	1 bar	15–60	9.62×10^{-3}	-1.92×10^{-1}	2.87×10^{-2}	0.96	3	Data obtained together with Fe-rich samples
Bi	FeS	1673	1 bar	5–120	8.18×10^{-3}	-1.64×10^{-1}	3.24×10^{-2}	0.79	8	Data obtained for FeS-rich samples only
Bi	FeS	1773	1 bar	5–60	1.13×10^{-2}	-2.26×10^{-1}	5.04×10^{-2}	0.83	5	Data obtained together with Fe-rich samples
Bi	FeS	1773	1 bar	5–60	1.54×10^{-2}	-3.08×10^{-1}	6.31×10^{-2}	0.77	8	Data obtained for FeS-rich samples only
Bi	FeS	1673	vacuum	15–60	$>1.44 \times 10^{-2}$	-2.88×10^{-1}	1.02×10^{-1}	0.80	3	Data obtained for FeS-rich samples only
Bi	FeS	1673	vacuum	15–30	$>2.58 \times 10^{-2}$	-5.16×10^{-1}	1.41×10^{-1}	0.93	2	Data obtained for FeS-rich samples only; removed 60 min exp
Bi	Fe	1673	1 bar	15–60	$>9.32 \times 10^{-3}$	-1.86×10^{-1}	5.20×10^{-2}	0.87	3	Data obtained together with FeS-rich samples
Bi	Fe	1673	1 bar	5–120	$>5.11 \times 10^{-3}$	-1.02×10^{-1}	3.52×10^{-2}	0.63	6	Data obtained for Fe-rich samples only

Table 3 (*continued*)

	Comp.	T (K)	Pressure	Time range (min)	k_i (cm/min)	Slope	1SE	R^2	N	Comment
Bi	Fe	1773	1 bar	5–60	$>1.09 \times 10^{-2}$	-2.18×10^{-1}	7.07×10^{-2}	0.70	5	Data obtained together with FeS-rich samples
Bi	Fe	1773	1 bar	5–60	$>1.37 \times 10^{-2}$	-2.75×10^{-1}	8.68×10^{-2}	0.59	8	Data obtained for Fe-rich samples only
Bi	Fe	1673	vacuum	15–60	$>1.09 \times 10^{-2}$	-2.19×10^{-1}	8.47×10^{-2}	0.77	3	Data obtained for Fe-rich samples only
Bi	Fe	1773	vacuum	5–60	$>1.20 \times 10^{-2}$	-2.40×10^{-1}	9.54×10^{-2}	0.61	5	Data obtained for Fe-rich samples only

for Fe melts from this study instead shows that at 1 bar and 1773 K the sequence is Bi, Pb, Cd, Te < Zn, In, Sn, Ag < Ge < S<Cu, Ga, Se, Sb (Fig. 5). At 0.0002 bar and 1673 K, the sequence is Zn, Ga, Sb, Sn, Cd, Te, Pb, Bi < Cu, Ge, Se, Ag < S (Fig. 5). However, as previously mentioned, the evaporation rates of the most volatile elements are likely lower limits due to near-complete evaporation. The overall differences to the commonly assumed 50 % condensation temperature sequence are thus (1) the higher-than-expected evaporation rate of Sb, i.e., being similarly volatile as elements with a much lower 50 % condensation temperature (S, Se) and (2) a much lower-than-expected evaporation rate of Se (i.e., less volatile than elements with much higher condensation temperatures) from Fe melt (Fig. 5). Tellurium also is significantly more volatile than Se, despite only a small difference in 50 % condensation temperatures (Fig. 5). Evaporation of a S-poor Fe melt would thus result in a relative increase of the Se/Te of the residue.

For FeS melt at a vacuum of 0.0002 bar, the following volatility sequence is derived: Te, Sn, Cd, Pb, In, Bi < Ga, Sb, Zn < Cu S. Sulfur and Se are thus among the least volatile elements in FeS melt (Fig. 6). The reaction rate constants were also compared with other commonly used volatility proxies, such as heat of vaporization, specific heat capacity and elemental boiling points. For both the FeS and Fe series, the reaction rate constants only correlate to some extent with the specific heat capacity (Fig. S2), but overall, poorly with elemental heat of vaporization values or boiling points. A comparison of the new results with traditionally applied volatility models based on condensation temperatures therefore confirms that the latter models are only partly applicable to constrain evaporative loss (Norris and Wood, 2017) and do not accurately describe evaporative loss from metallic melts (Steenstra et al., 2023).

In comparison with previous experimental studies on elemental evaporation from silicate melts (Norris and Wood, 2017; Sossi et al., 2019), our experimental results highlight significant differences between both systems (Fig. 7). At the most reduced conditions of the experiments of Norris and Wood (2017), corresponding to approximately 3 log units below the iron-wüstite buffer at 1573 K, they found a relative volatility factor sequence of Sb > Bi > Ge > Cd > Ag > Sn > Tl > Pb > Zn > Cu > In > Ga > Cr, with Sb being the most volatile at these conditions.

This sequence is significantly different from the volatility sequences obtained for both FeS and Fe melts (Steenstra et al., 2023, this study). For example, Sb is found to be significantly less or even non-volatile at 1673 K, whereas in silicate systems it is quite volatile (Fig. 7). Tin and Cd are significantly more volatile in our experiments, compared to experiments conducted at 1573 K with a silicate bulk composition (Fig. 7). Other notable differences include a much lower volatility of Cu in our experiments, despite the higher temperatures of the experiments (Fig. 7). Besides parental bulk composition, such differences may also be the result of the significantly different oxygen fugacities of the experiments (Norris and Wood, 2017; Sossi et al., 2019; Steenstra et al., 2023). Indeed, the oxygen fugacity imposed on the samples due to the use of graphite capsules and/or CO (~GCO buffer) is much more reduced compared to the previous experiments (i.e., ~ <5 units below the iron-wüstite buffer or ΔIW−5, compared to > ΔIW−3 of the considered experiments of Norris and Wood, 2017; Sossi et al., 2019) and potentially

more reduced compared to magmatic differentiation of asteroidal parent body cores. As described in section 3.2.4, such differences could affect the volatility of several elements, although this remains poorly constrained. It should also be noted that the volatilities of some elements in our experiments may be affected by the (trace) abundance of other elements that were simultaneously studied (e.g., Renggli and Klemme, 2020). For example, thermodynamic and experimental results indicate the potential presence of species such as CdTe, PbTe and CuTe. Thus, future experimental projects should be aimed at additionally constraining metal speciation and the effects of oxygen fugacity on the evaporation behavior from metallic melts.

4.2. Geochemical consequences of evaporation on volatile element systematics

The process(es) responsible for volatile element depletions in magmatic iron meteorites remain highly debated. This is also a direct result of relatively poor constraints on indigenous volatile element abundances in the various magmatic iron meteorite suites of interest. Nevertheless, the potential elemental depletion of (a) putative evaporation event(s) on magmatic iron meteorite parent bodies can now be assessed using our new experimental results in conjunction with assumed bulk meteorite measurements. For several elements (e.g., Zn, Cd, Sn, Te, Pb), the effects of magmatic differentiation within the meteorite suite can therefore not be assessed, and in some cases the concentrations of these elements in troilite were considered to represent the upper limit of their abundance in the magmatic iron meteorite suite as described below. By combining our new experimental results with previous modeling results (Steenstra et al., 2023), a quantitative estimate of their depletions after evaporation can be made. In the latter study, we showed that the inferred depletions of Cu, Ag and/or Ge in the IVB suite, relative to CI chondrites (Braukmüller et al., 2018; Alexander, 2019) can be largely if not fully explained by evaporation of a S-free or S-poor Fe melt at asteroid-relevant temperatures (i.e., 1673–1773 K) under a vacuum of 0.0004 bar at relatively short timescales (minutes to hour(s)). Here, we calculated the expected depletions of the elements of interest by assuming these conditions, in conjunction with the parameterizations listed in Table 2. We compare the calculated depletions with – where available – volatile element abundances from the literature for various magmatic iron meteorite classes. Elemental abundances of Ga are relatively well constrained in magmatic iron meteorites and have been inferred for the IVB parental melt in previous studies (Campbell and Humayun, 2005; Zhang et al., 2022). Zhang et al. (2022) also calculated the Sb content of the IVB parental melt, 8.2 ng/g, based on an extensive set of new bulk measurements of IVB magmatic iron meteorites. This value is close to the value of 3.3 ng/g estimated earlier by Wasson and Richardson (2001) for the IVA suite parental melt. Of the elements considered here and in our previous study (Steenstra et al., 2023), S, Cr, Co, Ni, Cu, Ga, Ge, Mo, Ru, Pd, Ag, Sb, W, Re, Ir are thus reconstructed abundances for the IVA (S) and IVB (all other elements) parental melts.

For the other elements considered here (Zn, Cd, Sn, Te, Pb), only few data are available and either bulk group IIAB (Sn, Te) and/or IVA (troilite) phase measurements were considered. These values are simply
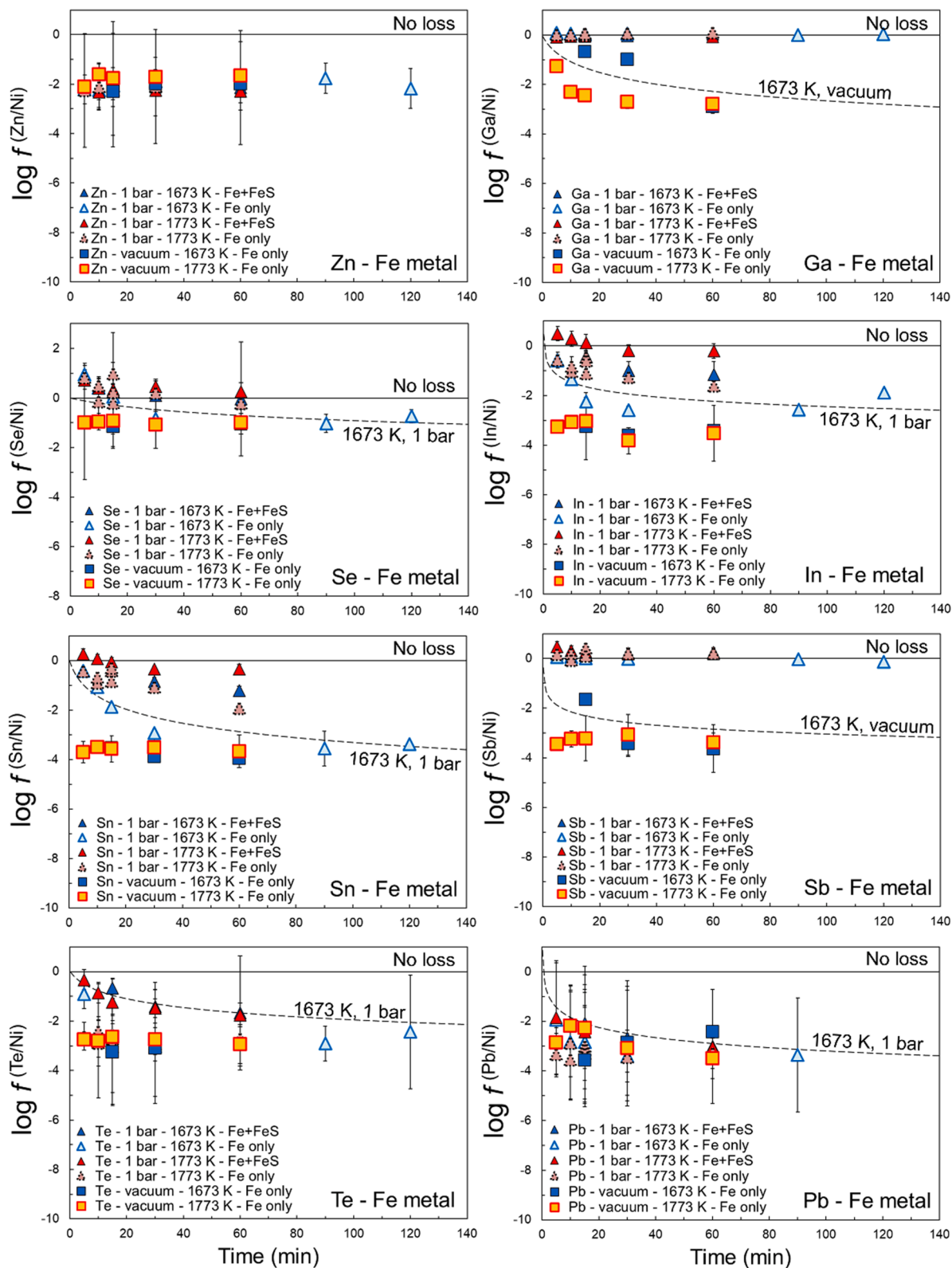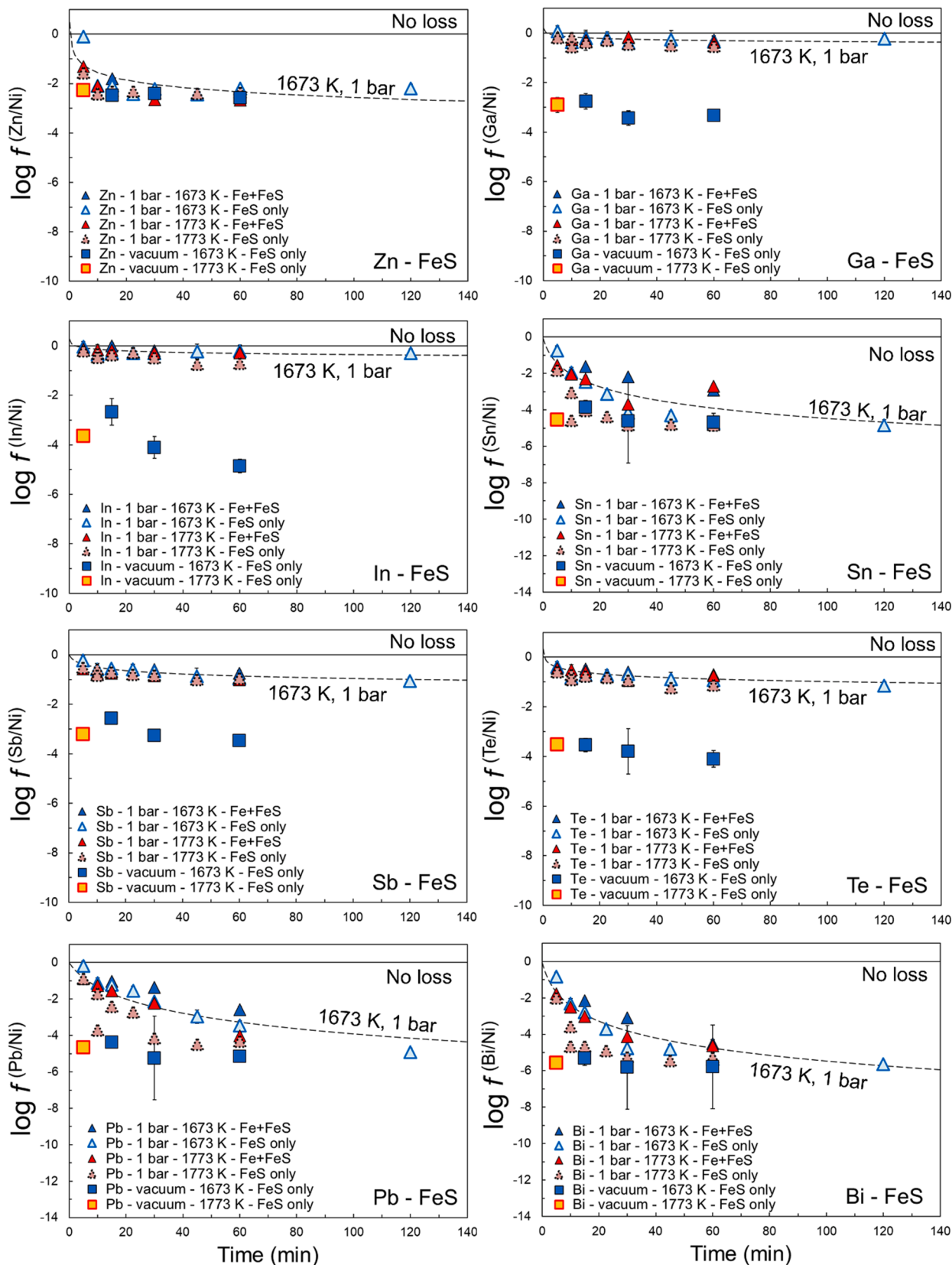
Fig. 3. Examples of evaporative loss factors (Eq. (1) depicted as a function of experimental run time for Fe liquids. The solid lines indicate the initial ratio prior to evaporation of the starting materials. The error bars represent maximum errors and were based on the uncertainties on the measured abundances by LA-ICP-MS in both the high-pressure melted starting composition and evaporated samples. Note that there are significant differences in the relative size of the associated errors bars, which is a result of inter-elemental differences in initial concentrations and the degree of polyatomic interferences (e.g., Burney and Neal, 2019). Dashed lines show the modeled dependencies detailed in Table 2 (where available). The data labels provide additional details related to the experimental set-up: if the experiment was conducted together with a Fe or FeS sample or if it was performed without another sample present.

Fig. 4. Examples of evaporative loss factors (Eq. (1) depicted as a function of experimental run time for FeS liquids. See Fig. 3 caption for additional details.
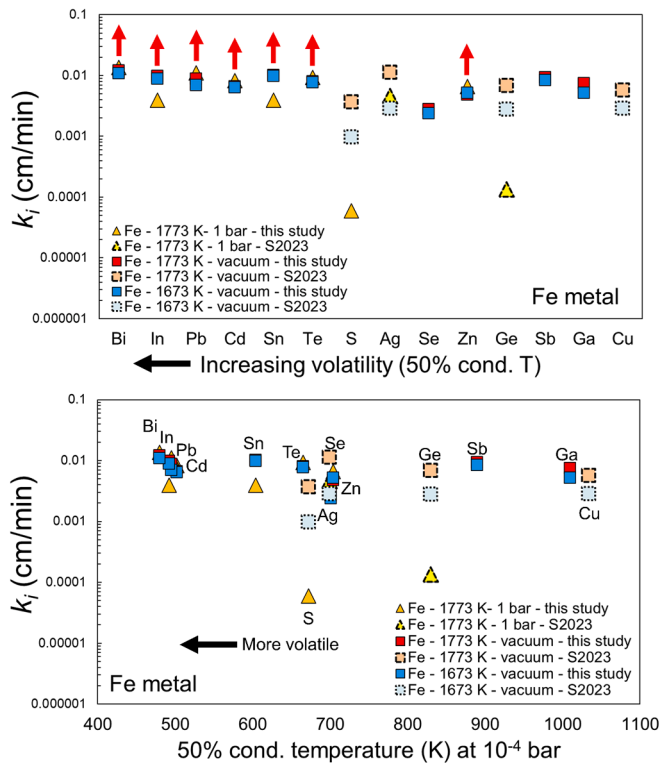
Fig. 5. Elemental reaction rate constants k_i for Fe samples at different pressures (vacuum, 1 bar) and temperatures (1673 or 1773 K) from this study and Steenstra et al. (2023) plotted in relative and absolute sequence of their 50 % condensation temperatures at 10^{-4} bar for a solar gas composition (Wood et al., 2019). The upward red arrows in the top panel indicate that the derived k_i values represent minimum values, as the latter elements exhibit extreme evaporation and their true k_i values could not be derived.

plotted to illustrate the observed depletion in the magmatic iron meteorite class that is closest to the IVA and/or IVB group. We do acknowledge that this should be considered as an upper limit abundance in their parent body and that in reality they must be significantly more depleted in the meteoritic bulk parent bodies. For Se, In, Bi, no bulk meteorite data for IV group magmatic iron meteorites, or any of the more volatile element depleted classes, are available at all, to our knowledge. We can simply only present the minimum depletions to be expected from evaporation for these elements. Chen et al. (2013) analyzed two IVA meteorites (Gibeon, Yanhuitlan) for Zn and obtained an average concentration of 0.42 ± 0.25 µg/g. Walker et al. (2008) analyzed several IVB iron meteorites using LA-ICPM and reported Zn concentrations of mostly <0.7 µg/g that were generally below or close to the LA-ICP-MS detection limit. Blichert-Toft et al. (2010) analyzed two IVA iron meteorites (Muonionalusta, Gibeon) for trace elements, including Pb, and obtained bulk meteorite concentrations that were quite variable (0.0077 $\pm$ 0.0074 µg/g to 0.097 $\pm$ 0.24 µg/g Pb). We therefore assumed the lower value for our modeling. This value is also close to Pb concentrations measured in troilite from Muonionalusta of 8 to 18 ng/g (Brennecka et al., 2018). The data for all many volatile elements in IVB irons, and by extension other magmatic iron meteorites, are scarce. In terms of Te and Sn, only a handful data exist for magmatic iron meteorites. Fehr et al. (2005) analyzed a single meteorite from two different magmatic iron meteorite groups for Te and Sn contents (IC, IIAB). For Te and Sn, we therefore assumed the average of the reported bulk IIAB concentrations in our model (Fig. 8). Measurements of Bi and Cd are also scarce in the literature and were mostly obtained using neutron activation analyses of troilite phases (e.g., Reed et al., 1960). More recent analyses by Kruijer et al. (2014) confirmed that Cd is strongly depleted in all magmatic iron meteorite groups and the reported analyses of two
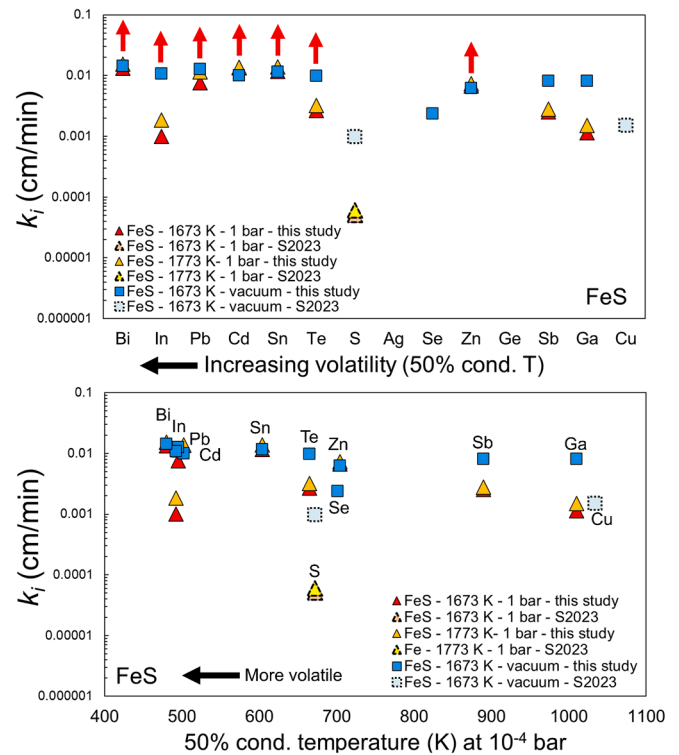
Fig. 6. Elemental reaction rate constants k_i for FeS samples at different pressures (vacuum, 1 bar) and temperatures (1673 or 1773 K) from this study and Steenstra et al. (2023) plotted in relative and absolute sequence of their 50 % condensation temperatures at 10^{-4} bar for a solar gas composition (Wood et al., 2019). See Fig. 5 caption for additional details.
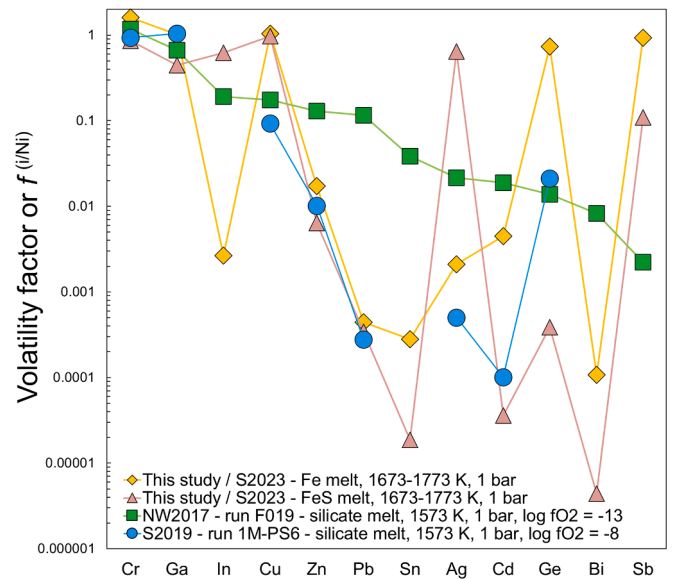

Fig. 7. A comparison between volatility factors for silicate melts (Norris and Wood, 2017; Sossi et al., 2019; obtained at a run time of 60 min) with evaporative loss factors, normalized to Ni, from this study (experiments ESS-140C1 Fe and ESS-140C FeS) and Steenstra et al. (2023) (experiments CRESS-7 Fe and CRESS-7 FeS, conducted for 60 min at 1773 K).

IVA troilite phases were used for comparison purposes (Fig. 8).

As previously noted, the abundances of Zn, Se, Cd, Sn, Te, Pb were based on bulk meteorite measurements and do not account for potential silicate melt, metal and/or sulfide melt fractionation. It is expected that
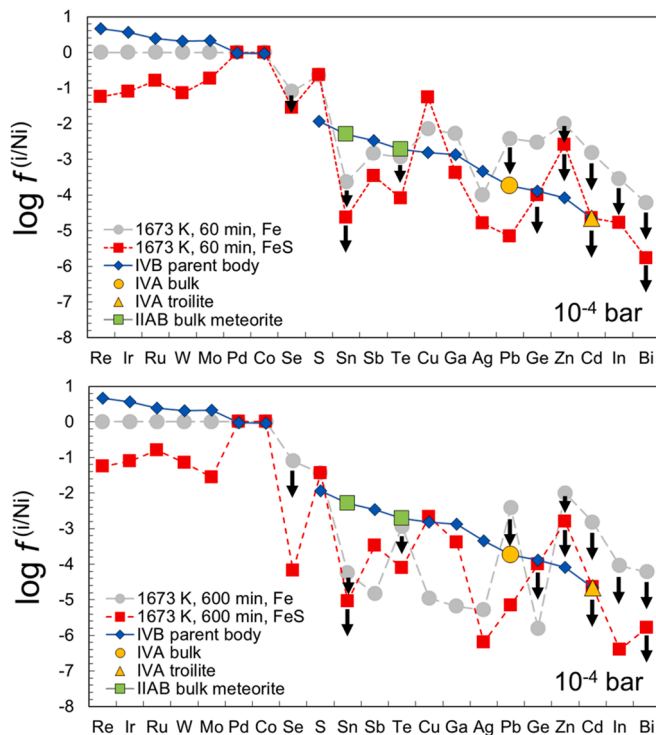
Fig. 8. Comparison between reconstructed IVB parent melt compositions (where available; Chabot, 2004, Campbell and Humayun, 2005; Zhang et al., 2022; Steenstra et al., 2023), relative to a CI chondritic bulk composition (Braukmüller et al., 2018 for Cd, Pb; Alexander, 2019 for all other elements, e.g., Zhang et al., 2022), with modeled Ni-normalized evaporative loss factors. The Ni-normalized evaporative loss factors were calculated for 1673 and 1773 K, under vacuum, for Fe or FeS melt, while assuming an evaporation time of 60 and 600 min, respectively (Steenstra et al., 2023). The elemental concentrations of Zn, Cd, Sn and Te do not represent reconstructed parental IVA or IVB melt compositions and are taken from a wider range of magmatic iron meteorite groups due to an overall lack of data. The bulk concentration of Zn was based on measurements of Zn in two IVA meteorites (Gibeon, Yanhuitlan; Chen et al., 2013). The abundances of Sn and Te were based on average bulk meteorite concentrations of the IIAB meteorite North Chile (N = 2; Fehr et al., 2005), because no data for IVA or IVB meteorites are available. The Cd abundance is based on measurements of troilite nodules of two IVA meteorites (Gibeon and Muonionalusta, Kruijer et al., 2014). For Pb, the lowest value measured in troilite of Muonionalusta was used (Blichert-Toft et al., 2010). For Se, In and Bi, no data is available to our knowledge for IVA or IVB compositions, nor for any magmatic iron meteorite groups that show a significant depletion in volatile elements. Downward arrows indicate that the expected depletion is likely more significant due to the issues of measuring the elements of interest at very low concentrations in the experimentally evaporated samples.

most elements considered are either partitioned largely if not solely into FeS melt (Zn, Cd, In, Te, Pb, Bi) or to a similar extent in both FeS and Fe liquid (Ga, Sn, Sb), throughout the oxygen fugacity range applicable to asteroidal differentiation (e.g., Steenstra et al., 2017; 2020b). Thus, only a very minor fraction of the volatile elements considered here would have partitioned into the co-existing silicate melt during parent body differentiation. However, significant fractionation between solid metal and liquid metal of most volatile elements considered here is expected. Most elements considered here prefer liquid over solid metal, with $D^{solid}_{metal/liquid\ metal}$ values ranging commonly between ~0.01 to 1, the magnitude depending particularly of the composition in terms of C, P and S (e.g., Chabot and Jones, 2003; Rai et al., 2013; Chabot et al., 2017). Both solid metal − liquid metal and/or subsequent immiscibility of a S-rich melt from a S-poor melt would have additionally enriched most elements in the liquid metal and/or sulfide melt. Therefore, the considered bulk meteorite measurements represent the upper limit of

their expected abundances in bulk magmatic iron meteorite parent bodies.

Evaporation, even at the lowest temperatures and for short durations, should have resulted in an extreme depletion of Cd and Bi (>99.5 %), in both S-free and S-rich systems (Fig. 8). Kruijer et al. (2014) concluded from the measured depletions that all known magmatic iron meteorite parent bodies must have accreted at temperatures much higher than the $T_{50\%}$ temperature of Cd of ~500 to ~650 K (Lodders, 2003; Wood et al., 2019). Available Cd abundances can thus be easily reconciled with both evaporation (Fig. 8) and/or incomplete condensation, especially given the fact that the data for both systems represent minimum evaporation rates given the highly volatile behavior of Cd in the experiments (Figs. 3 and 4). Bridgestock et al. (2014) measured and compiled Zn abundance and isotopic data of the non-magmatic iron meteorite group IAB and magmatic iron meteorite groups IIAB and IIIAB. They concluded that the observed Zn systematics were not a consequence of metal crystallization but instead reflect (a) different local process(es), most likely chromite crystallization and segregation, with no clear evidence of evaporative loss. The new data shows that any degree of evaporation would strongly deplete Zn, at least several orders of magnitude (Fig. 8). As for Cd, the modeled extent of Zn evaporation from both Fe and FeS liquid is likely underestimated due to its highly volatile nature in the experiments (Figs. 3 and 4).

Previous workers concluded that Pb was largely absent prior to crystallization of magmatic iron meteorites, for example in the case of the Steinbach anomalous stony-iron group IVA meteorite (Connelly et al., 2019). They hypothesized that Pb was most likely lost during impact of the parent body but prior to re-accretion of the parent body debris. The modeled evaporation at 1673–1773 K at a vacuum of 0.0002 bar indicates that Pb would at least be depleted 2–5 orders of magnitude, depending on metal composition (Fig. 8). The volatility of Pb in Fe liquid is likely much higher than inferred here, given the difficulties of measuring Pb at the low concentrations in some of the experiments. However, the results show that the observed depletion of Pb in IVA bulk meteorites can be easily reconciled with (an) evaporation event(s). Similar results are found for both Ga and Sb. Evaporation under the explored conditions from both FeS or Fe liquid yields a depletion that is within the range of sample observations (Fig. 8). Evaporation at 1673–1773 K under a vacuum of 0.0002 yields expected depletions of Te and Sn for both Fe and FeS melts that are generally much larger than their observed depletions in the IIAB group (Fig. 8). Given that the latter Sn and Te contents were based on IIAB group magmatic iron meteorite measurements (Fehr et al., 2005), due to lack of data, their actual depletions in the IVB are likely to be much greater given the depletion trends observed for other volatile elements among the different classes (e.g., Ga, Ge; Goldstein et al., 2009). Although there are no bulk meteorite measurements of Se and In with which our modeled evaporation behavior can be compared, the results do show that evaporation would yield significant depletions of Se and In within the explored conditions (i.e., up to 4–5 log units depending on composition, temperature and time). Finally, our results also show that evaporation of a partially liquid parental body core would yield comparable depletions of the considered volatile elements, relative to a fully liquid core (see section 3.2.1).

Altogether, the new evaporation models show that evaporation could yield much of the observed volatile element abundances in the most volatile element-depleted magmatic iron meteorite suites. However, for many elements it is difficult to differentiate, at least now, between processes of incomplete condensation or evaporative loss, due to their extremely volatile behavior (e.g., Cd). To provide more context to our models, we therefore recommended that future work is required to better constrain the indigenous bulk meteorite abundances of most volatile elements considered here, because they are often insufficiently or even poorly constrained. Finally, the exact reaction rates or degrees of depletion of the most volatile elements could be better constrained by using much higher initial abundances, which most likely would require experiments to be conducted individually for each element.

5. Conclusions

The volatilities of most volatile metals during evaporation of S-free/poor and S-bearing metallic melts were experimentally assessed. The results confirm the previously proposed importance of S for elemental evaporation from metallic melts. This depends largely on the S-avoiding or S-loving behavior for the element of interest, as defined by the effect of S on its thermodynamic activity in a metallic melt. The newly derived elemental volatility sequences are distinctly different relative to volatility sequence expected during elemental condensation. The experiments also show that a metal body, or a remnant of a protoplanetary core, does not require complete melting to significantly evaporate volatile metals, increasing the potential of evaporative loss on asteroidal parent bodies. The newly derived (minimum) reaction rates and volatility sequences provide a thermodynamic and geochemical framework that are required for distinguishing between the various volatile element depletion mechanisms, but its application is currently limited by the availability of bulk elemental measurements of magmatic iron meteorites. Future work should better constrain the indigenous bulk abundances of several of the elements of interest in magmatic iron meteorites. The potential of elemental evaporation on magmatic iron meteorite parent bodies, and the relative importance of incomplete condensation, can then be assessed in much greater detail.

Data Availability

Data are available through Mendeley Data at https://doi.org/10.17632/99r448mw9j.1.

CRediT authorship contribution statement

E.S. Steenstra: Writing – review & editing, Writing – original draft, Validation, Project administration, Methodology, Investigation, Funding acquisition, Formal analysis, Conceptualization. **C.J. Renggli:** Writing – review & editing, Methodology, Investigation, Conceptualization. **J. Berndt:** Writing – review & editing, Methodology, Formal analysis. **S. Klemme:** Writing – review & editing, Supervision, Resources, Funding acquisition.

Declaration of competing interest

The authors declare that they have no known competing financial interests or personal relationships that could have appeared to influence the work reported in this paper.

Acknowledgements

Appendix A. Supplementary material

The Supplementary Material file contains additional information regarding potential cross-contamination of samples and a summary of the chemical analyses of the experimental samples conducted with EPMA and LA-ICP-MS. Supplementary material to this article can be found online at https://doi.org/10.1016/j.gca.2024.08.021.

References

Alexander, C.M.O'D., 2019. Quantitative models for the elemental and isotopic fractionations in chondrites: the carbonaceous chondrites. Geochim. Cosmochim. Act. 254, 277–309.

Blichert-Toft, J., Moynier, F., Lee, C.-T.-A., Telouk, P., Albarede, F., 2010. The early formation of the IVA iron meteorite parent body. Earth Planet. Sci. Lett. 296, 469–480.

Braukmüller, N., Wombacher, F., Hezel, D.C., Escoube, R., Münker, C., 2018. The chemical composition of carbonaceous chondrites: implications for volatile element depletion, complementarity and alteration. Geochim. Cosmochim. Act. 239, 17–48.

Brennecka, G.A., Amelin, Y., Kleine, T., 2018. Uranium isotope ratios of Muonionalusta troilite and complications for the absolute age of the IVA iron meteorite core. Earth Planet. Sci. Lett. 490, 1–10.

Bridgestock, L.J., Williams, H., Rehkämper, M., Larner, F., Giscard, M.D., Hammond, S., et al., 2014. Unlocking the zinc isotope systematics of iron meteorites. Earth Planet. Sci. Lett. 400, 153–164.

Buono, A.S., Walker, D., 2011. The Fe-rich liquidus in the Fe-FeS system from 1 bar to 10 GPa. Geochim. Cosmochim. Act. 75, 2072–2087.

Burney, D., Neal, C.R., 2019. Method for quantifying and removing polyatomic interferences on a suite of moderately volatile elements (Zn, Se, Rb, Ag, Cd, In, Sb, Tl, Pb, and Bi) during solution-mode ICP-MS. J. Anal. at. Spectrom. 34, 1856–1864.

Campbell, A.J., Humayun, M., 2005. Compositions of group IVB iron meteorites and their parent melt. Geochim. Cosmochim. Act. 69 (19), 4733–4744.

Chabot, N.L., 2004. Sulfur contents of the parental metallic cores of magmatic iron meteorites. Geochim. Cosmochim. Act. 68, 3607–3618.

Chabot, N.L., Haack, H., 2006. Evolution of asteroidal cores. Meteorites Early Solar Syst. II, 747–771.

Chabot, N.L., Jones, J.H., 2003. The parameterization of solid metal-liquid metal partitioning of siderophile elements. Meteorit. Planet. Sci. 38 (10), 1425–1436.

Chabot, N.L., Wollack, E.A., McDonough, W.F., Ash, R.D., Saslow, S.A., 2017. Experimental determination of partitioning in the Fe-Ni system for application to modeling meteoritic metals. Meteorit. Planet. Sci. 52, 1133–1145.

Chabot, N.L., Zhang, B., 2021. A revised trap melt model for iron meteorites applied to the IIIAB group. Meteorit. Planet. Sci. 1–28.

Chen, H., Nguyen, B.M., Moynier, F., 2013. Zinc isotopic composition of iron meteorites: absence of isotopic anomalies and the origin of the volatile element depletion. Meteorit. Planet. Sci. 48, 2441–2450.

Connelly, J.N., Schiller, M., Bizzarro, M., 2019. Pb isotope evidence for rapid accretion and differentiation of planetary embryos. Earth Planet. Sci. Lett. 525, 115722.

Corgne, A., Wood, B.J., Fei, Y., 2008. C- and S-rich molten alloy immiscibility and core formation of planetesimals. Geochim. Cosmochim. Act. 72, 2409–2416.

Corrigan, C.M., Kagashima, K., Hilton, C., McCoy, T.J., Ash, R.D., Tornabene, H.A., Walker, R.J., McDonough, W.F., Rumble, D., 2022. Nickel-rich, volatile depleted iron meteorites: relationships and formation processes. Geochim. Cosmochim. Act. 333, 1–21.

Fehr, M.A., Rehkämper, M., Halliday, A.N., Wiechert, U., Hattendorf, B., Günter, D., Ono, S., Eigenbrode, J.L., Rumble III, D., 2005. Tellurium isotopic composition of the early solar system – a search for effects resulting from stellar nucleosynthesis, 126Sn decay, and mass-independent fractionation. Geochim. Cosmochim. Act. 69, 5099–5112.

Flemetakis, S., Renggli, C.J., Pangritz, P., Berndt, J., Klemme, S., 2024. Evaporation of Boron from aluminoborosilicate melt. Eur. J. Min. 36, 173–181.

Gargano, A., Sharp, Z., 2019. The chlorine isotope composition of iron meteorites: evidence for the Cl isotope composition of the solar nebula and implications for extensive devolatilization during planet formation. Meteorit. Planet. Sci. 54, 1619–1631.

Goldstein, J.I., Scott, E.R.D., Chabot, N.L., 2009. Iron meteorites: crystallization, thermal history, parent bodies, and origin. Chemie Der Erde - Geochemistry 69, 293–325.

Grewal, D.S., Asimow, P.D., 2023. Origin of the superchondritic carbon/nitrogen ratio of the bulk silicate Earth – an outlook from iron meteorites. Geochim. Cosmochim. Act. 344, 146–159.

Grewal, D.S., Nie, N.X., Zhang, B., Izodoro, A., Asimow, P.D., 2024. Accretion of the earliest inner solar system planetesimals beyond the water snowline. Nat. Astron. 8, 290–297.

Griffin, W.L., Powell, W.J., Pearson, N.J., O'Reilly, S.Y., 2008. GLITTER: data reduction software for laser ablation ICP-MS, in Sylvester P, ed., Laser Ablation ICPMS in the Earth Sciences: current Practices and Outstanding Issues, Mineralogical Association of Canada. Short Course Series 40, 308–311.

Haack, H., Scott, E.R.D., Love, S.G., Brearley, A., 1996. Thermal histories of IVA stony-iron and iron meteorites: Evidence for asteroid fragmentation and reaccretion. Geochim. Cosmochim. Act. 60, 3103–3113.

Hirschmann, M.M., Bergin, E.A., Blake, G.A., Ciesla, F.J., Li, J., 2021. Early volatile depletion on planetesimals inferred from C-S systematics of iron meteorite parent bodies. Proc. Nat. Ac. Sci. 118 (13), e2026779118.

Horan, M.F., Carlson, R.W., Blichert-Toft, J., 2012. Pd-Ag chronology of volatile depletion, crystallization and shock in the Muonionalusta IVA iron meteorite and implications for its parent body. Earth Planet. Sci. Lett. 351–352, 215–222.

Ivanova, M.A., Mendybaev, R.A., Shornikov, S.I., Lorenz, C.A., MacPherson, G.J., 2021. Modeling the evaporation of CAI-like melts, and constraining the origin of CH-CB CAIs. Geochim. Cosmochim. Act. 296, 97–116.

Jochum, K.P., Nohl, U., Herwig, K., Lammel, E., Stoll, B., Hofmann, A.W., 2005. GeoReM: a new geochemical database for reference materials and isotopic standards. Geost. Geoanal. Res. 29, 333–338.

Jordan, M.K., Tang, H., Kohl, I.E., Young, E.D., 2019. Iron isotope constraints on planetesimal core formation in the early solar system. Geochim. Cosmochim. Act. 246, 461–477.

Kruijer, T.S., Sprung, P., Kleine, T., Leya, I., Wieler, R., 2014. The abundance and isotopic composition of Cd in iron meteorites. Meteorit. Planet. Sci. 48 (12), 2597–42607.

Lodders, K., 2003. Solar system abundances and condensation temperatures of the elements. Astrophys. J. 591, 1220.

Matthes, M., Fischer-Gödde, M., Kruijer, T.S., Kleine, T., 2018. Pd-Ag chronometry of IVA iron meteorites and the crystallization and cooling of a protoplanetary core. Geochim. Cosmochim. Act. 220, 82–95.

Matthes, M., van Orman, J.A., Kleine, T., 2020. Closure temperature of the Pd-Ag system and the crystallization ages and cooling history of the IIIAB iron meteorites. Geochim. Cosmochim. Act. 285, 193–206.

Ni, P., Chabot, N.L., Ryan, C.J., Shahar, A., 2020. Heavy iron isotope composition of iron meteorites explained by core crystallization. Nat. Geosci. 13 (9), 611–615.

Norris, A., Wood, B.J., 2017. Earth's volatile contents established by melting and vaporization. Nature 549, 507–510.

Rai, N., Ghosh, S., Wälle, M., van Westrenen, W., 2013. Quantifying the effect of solid phase composition and structure on solid-liquid partitioning of siderophile and chalcophile elements in the iron-sulfur system. Chem. Geol. 357, 85–94.

Rasmussen, K.L., Malvin, D.J., Buchwald, V.F., Wasson, J.T., 1984. Compositional trends and cooling rates of group IVB iron meteorites. Geochim. Cosmochim. Act. 48, 805–813.

Reed, G.W., Kigoshi, K., Turkevich, A., 1960. Determinations of concentrations of heavy elements in meteorites by activation analysis. Geochim. Cosmochim. Act. 20, 122–140.

Renggli, C.J., Klemme, S., 2020. Experimental constraints on metal transport in fumarolic gases. J. Volcan. Geotherm. 400, 106929.

Renggli, C.J., Hellman, J.L., Burkhardt, C., Klemme, S., Berndt, J., Pangritz, P., Kleine, T., 2022. Tellurium isotope fractionation during evaporation from silicate melts. Geochim. Cosmochim. Act. 339, 35–45.

Righter, K., Pando, K., Humayun, M., Waeselmann, N., Yang, S., Boujibar, A., Danielson, L.R., 2018. Effect of silicon on activity coefficients of siderophile elements (Au, Pd, Pt, P, Ga, Cu, Zn, and Pb) in liquid Fe: roles of core formation, late sulfide matte, and late veneer in shaping terrestrial mantle geochemistry. Geochim. Cosmochim. Act. 232, 101–123.

Rubin, A.E., 2018. Carbonaceous and noncarbonaceous iron meteorites: differences in chemical, physical, and collective properties. Met. Planet. Sci. 53 (11), 2357–2371.

Rubin, A.E., Zhang, B., Chabot, N.L., 2022. IVA iron meteorites as late-stage crystallization products affected by multiple collisional events. Geochim. Cosmochim. Act. 331, 1–17.

Scott, E.R.D., 1979. Origin of anomalous iron meteorites. Mineral. Mag. 43, 415–421.

Scott, E.R.D., Wasson, J.T., 1975. Classification and properties of iron meteorites. Rev. Geophys. 13, 527–546.

Sears, D.W., 1978. Condensation and the composition of iron meteorites. Earth Planet. Sci. Lett. 41, 128–138.

Sossi, P.A., Klemme, S., O'Neill, H., St, C., Berndt, J., Moynier, F., 2019. Evaporation of moderately volatile elements from silicate melts: experiments and theory. Geochim. Cosmochim. Act. 260, 204–231.

Spitzer, F., Burkhardt, C., Pape, J., Kleine, T., 2021. Collisional mixing between inner and outer solar system planetesimals inferred from the Nedagolla iron meteorite. Meteorit. Planet. Sci. 57, 261–276.

Steenstra, E.S., 2024. Research data file for ''Quantification of evaporative loss of highly volatile metals from planetary cores and metal-rich planetesimals''. Mendeley Data V1.

Steenstra, E.S., Sitabi, A.B., Lin, Y.H., Rai, Knibbe, J.S., Berndt, J., Matveev, S., van Westrenen, W., 2017. The effect of melt composition on metal-silicate partitioning of siderophile elements and constraints on core formation in the angrite parent body. Geochim. Cosmochim. Acta 212, 62–83.

Steenstra, E.S., Seegers, A.X., Putter, R., Berndt, J., Klemme, S., Matveev, S., Bullock, E. S., van Westrenen, 2020a. Metal-silicate partitioning systematics of siderophile elements at reducing conditions: a new experimental database. Icarus 355, 113391.

Steenstra, E.S., Trautner, V.T., Berndt, J., Klemme, S., van Westrenen, W., 2020b. Trace element partitioning between sulfide-, metal- and silicate melts at highly reduced conditions: insights into the distribution of volatile elements during core formation in reduced bodies. Icarus 335, 113408.

Steenstra, E.S., Renggli, C.R., Berndt, J., Klemme, S., 2023. Evaporation of moderately volatile elements from metal and sulfide melts: implications for volatile element abundances in magmatic iron meteorites. Earth Planet. Sci. Lett. 622, 118406.

Tsuchiyama, A., Nagahara, H., Kushiro, I., 1981. Volatilization of sodium from silicate melt spheres and its application to the formation of chondrules. Geochim. Cosmochim. Act. 45, 1357–1367.

Tuff, J., Wood, B.J., Wade, J., 2011. The effect of Si on metal-silicate partitioning of siderophile elements and implications for the conditions of core formation. Geochim. Cosmochim. Act. 75, 673–690.

van Achterbergh, E., Ryan, C.G., Jackson, S.E., Griffin, W.L., 2001. Data reduction software for LA-ICP-MS: appendix. In: Sylvester, P.J. (Ed.), Laser Ablation-ICP Mass Spectrometry in the Earth Sciences: Principles and Applications, vol. 29, Ottawa: Mineralog. Assoc. Canada (MAC) Short Course Series, pp. 239–243.

Wai, C.M., Wasson, J.T., 1979. Nebular condensation of Ga, Ge and Sb and the chemical classification of iron meteorites. Nature 282, 790–793.

Walker, R.J., McDonough, W.F., Honesto, J., Chabot, N.L., McCoy, T.J., Ash, R.D., Belluci, J.J., 2008. Modeling fractional crystallization of group IVB iron meteorites. Geochim. Cosmochim. Act. 72, 2198–2216.

Wasson, J.T., Richardson, J.W., 2001. Fractionation trends among IVA iron meteorites: contrasts with IIIAB trends. Geochim. Cosmochim. Act. 65, 951–970.

Wood, B.J., Kiseeva, E.S., Mirolo, F.J., 2014. Accretion and core formation: the effects of sulfur on metal-silicate partition coefficients. Geochim. Cosmochim. Act. 145, 248–267.

Wood, B.J., Smythe, D.J., Harrison, T., 2019. The condensation temperatures of the elements: a reappraisal. Am. Min. 104 (6), 844–856.

Yang, J., Goldstein, J.I., Scott, E.R., 2008. Metallographic cooling rates and origin of IVA iron meteorites. Geochim. Cosmochim. Act. 72 (12), 3043–3061.

Yang, J., Goldstein, J.I., Michael, J.R., Kotula, P.G., Scott, E.R., 2010. Thermal history and origin of the IVB iron meteorites and their parent body. Geochim. Cosmochim. Act. 74 (15), 4493–4506.

Yang, J., Fei, Y., Hu, X., Greenberg, E., Prakapenka, V.B., 2019. Effect of carbon on the volume of solid iron at high pressure: implications for carbon substitution in iron structures and carbon content in the Earth's Inner Core. Minerals 9, 720.

Zhang, B., Chabot, N.L., Rubin, A.E., 2022. Compositions of carbonaceous-type asteroidal cores in the early solar system. Sci. Adv. 8, eabo5781.